remote sensing

MDPI

Review

Current Status of Application of Spaceborne GNSS-R Raw Intermediate-Frequency Signal Measurements: Comprehensive Review

Qiulan Wang [1], Jinwei Bu [1,2,*], Yutong Wang [1], Donglan Huang [1], Hui Yang [1] and Xiaoqing Zuo [1,2]

[1] Faculty of Land Resources Engineering, Kunming University of Science and Technology, Kunming 650093, China; 202210108133@stu.kust.edu.cn (Q.W.); wangyutong@stu.kust.edu.cn (Y.W.); 202210108124@stu.kust.edu.cn (D.H.); 202310108143@stu.kust.edu.cn (H.Y.); zxq@kust.edu.cn (X.Z.)

[2] Yunnan Key Laboratory of Intelligent Monitoring and Spatiotemporal Big Data Governance of Natural Resources, Kunming 650093, China

* Correspondence: b_jinwei@kust.edu.cn

Abstract

In recent years, spaceborne Global Navigation Satellite System reflectometry (GNSS-R) technology has made significant progress in the fields of Earth observation and remote sensing, with a wide range of applications, important research value, and broad development prospects. However, despite existing research focusing on the application of spaceborne GNSS-R L1-level data, the potential value of raw intermediate-frequency (IF) signals has not been fully explored for special applications that require a high accuracy and spatiotemporal resolution. This article provides a comprehensive overview of the current status of the measurement of raw IF signals from spaceborne GNSS-R in multiple application fields. Firstly, the development of spaceborne GNSS-R microsatellites launch technology is introduced, including the ability of microsatellites to receive GNSS signals and receiver technique, as well as related frequency bands and technological advancements. Secondly, the key role of coherence detection in spaceborne GNSS-R is discussed. By analyzing the phase and amplitude information of the reflected signals, parameters such as scattering characteristics, roughness, and the shape of surface features are extracted. Then, the application of spaceborne GNSS-R in inland water monitoring is explored, including inland water detection and the measurement of the surface height of inland (or lake) water bodies. In addition, the widespread application of group delay sea surface height measurement and carrier-phase sea surface height measurement technology in the marine field are also discussed. Further research is conducted on the progress of spaceborne GNSS-R in the retrieval of ice height or ice sheet height, as well as tropospheric parameter monitoring and the study of atmospheric parameters. Finally, the existing research results are summarized, and suggestions for future prospects are put forward, including improving the accuracy of signal processing and reflection signal analysis, developing more advanced algorithms and technologies, and so on, to achieve more accurate and reliable Earth observation and remote sensing applications. These research results have important application potential in fields such as environmental monitoring, climate change research, and weather prediction, and are expected to provide new technological means for global geophysical parameter retrieval.

Keywords: spaceborne GNSS-R; raw intermediate-frequency signal; coherence detection; inland water body; sea surface height; ice sheet height; atmospheric parameters

check for updates

Academic Editors: Younghyun Cho, Taeil Jang and Won-Ho Nam

Received: 12 March 2025
Revised: 13 June 2025
Accepted: 18 June 2025
Published: 22 June 2025

Citation: Wang, Q.; Bu, J.; Wang, Y.; Huang, D.; Yang, H.; Zuo, X. Current Status of Application of Spaceborne GNSS-R Raw Intermediate-Frequency Signal Measurements: Comprehensive Review. *Remote Sens.* **2025**, *17*, 2144. https://doi.org/10.3390/rs17132144

Copyright: © 2025 by the authors. Licensee MDPI, Basel, Switzerland. This article is an open access article distributed under the terms and conditions of the Creative Commons Attribution (CC BY) license (https://creativecommons.org/licenses/by/4.0/).

1. Introduction

The continuous development of satellite navigation technology and the increasing number of satellite constellations have brought new opportunities for Global Navigation Satellite System reflectometry (GNSS-R). As an emerging passive remote sensing technology, it was first proposed in 1988 as bistatic scatterometry [1]. After continuous development over time, GNSS-R technology was first proposed for ocean altimetry in 1993 [2], and its feasibility has been proven through many ground-based and airborne experiments [3,4]. GNSS-R can be divided into ground-based GNSS-R, airborne GNSS-R, and spaceborne GNSS-R based on the installation location of the GNSS receiver. Compared with ground-based GNSS-R and airborne GNSS-R, spaceborne GNSS-R technology has unique advantages such as a short revisit period, high spatiotemporal resolution, and low observation cost. In addition, spaceborne GNSS-R uses L-band GNSS signals that can penetrate clouds and heavy rain [5], making it capable of all-weather observation.

The Disaster Monitoring Constellation (DMC), a low-Earth-orbit satellite constellation launched by the UK in 2003, first demonstrated the feasibility of spaceborne GNSS-R [6]. The successful launch of TechDemoSat-1 (TDS-1) in the UK in 2014 facilitated further research on spaceborne GNSS-R, such as sea surface height measurement [7], sea ice detection [8], ice sheet height measurement [9], and soil freezing and thawing [10]. However, the sparse data coverage and calibration issues of TDS-1 limited its data availability. The Cyclone Global Navigation Satellite System (CYGNSS) launched by the United States in 2016 was an important milestone in spaceborne GNSS-R. It is a satellite constellation consisting of eight low-Earth-orbit satellites, mainly responsible for monitoring tropical cyclones [11]. In addition, the successive launch of various spaceborne GNSS-R missions, such as Spain's 3Cat-5 A/B (FSSCat) [12], the European Space Agency's PRETTY [13], China's BuFeng-1 (BF-1) A/B [14], Fengyun-3 series satellites [15], Tianmu-1 constellation [16], and the Jilin-1 wide range 01B satellite (J1-01B) [17], and Muon Space (Muon) in the United States [18], as well as the upcoming launch of HydroGNSS [19], demonstrate the enormous potential of spaceborne GNSS-R technology.

The current spaceborne GNSS-R technology has been widely applied in various fields such as ocean [20] and land [16]. However, most studies are based on the generation of delay Doppler maps (DDMs) of direct and reflected signals as the main data products (referred to as level 1 or L1 data). The sampling rate of these power DDM products is usually 1 Hz (coherent integration time of 1 s), corresponding to a spatial sampling resolution of 6–8 km. However, in addition to standard data products, in order to explore other possible GNSS-R applications, optimize future spaceborne GNSS-R instruments, and develop new GNSS-R applications, some spaceborne GNSS-R missions also collect a large amount of raw intermediate-frequency (IF) signals, which are bit streams of raw signal samples recorded after analog-to-digital converters (ADCs) and prior to any onboard digital processing [21]. At present, the raw IF data of spaceborne GNSS-R has shown great potential in many geophysical applications and has provided important theoretical support for the design and optimization of spaceborne GNSS-R instruments. The detailed processing process can be found in references [21,22].

Li et al. have conducted extensive and in-depth research on the processing of spaceborne GNSS-R raw IF signals and their related applications. In 2017, Li et al. [23] achieved the first phase height measurement of sea ice using TDS-1 L0 raw samples, which showed a good consistency with the mean sea surface (MSS) model, with a root mean square difference (RMSD) of 4.7 cm. Subsequently, in 2018, they successfully applied altimetry to the Qinghai Lake water body using CYGNSS raw IF data, demonstrating the ability to measure inland water body altimetry using spaceborne GNSS-R raw IF data [24]. Mayers and Ruf [25] used a simulator to create raw IF data received by CYGNSS. This study differs

from previous research in that it only tracked the carrier phase of the reflected signal, and the results showed that the relative phase can be used to calculate ice thickness. In subsequent studies, Li et al. [22] evaluated sea surface altimetry using CYGNSS raw IF data and pointed out that using raw data can overcome the limitations of signal processing, data compression, and inaccurate or truncated delay variables in primary metadata. In 2020, Song et al. [26] studied a height measurement method based on bistatic group delay using raw IF data received by TDS-1. The results showed that the model was consistent with the MSS model, and correcting GNSS-R satellite orbit errors through the MSS and least squares solutions could improve the deficiencies of level 1 data. This study provides a reference for using spaceborne GNSS-R raw IF data for height measurement. In 2021, Wang and Morton [27] introduced an adaptive hybrid carrier tracking algorithm (AHT) suitable for processing coherent GNSS-R signals. AHT combines Doppler models with adaptive closed-loop (ACL) tracking, integrating master–slave open-loop (MS-OL) and closed-loop (CL) carrier-phase tracking systems, with a high accuracy and robustness, without the need for precise initialization. The article utilized CYGNSS raw IF data to study inland water, terrestrial, and open sea surfaces, demonstrating the excellent performance of AHT in these scenarios, especially in measuring ocean height, achieving centimeter-level high-precision ocean height measurement. In addition, AHT can also improve GNSS-R land applications and can be applied to tracking other wireless signals. Wang et al. [28] proposed a state-based method to address the issue of inaccurate measurement results caused by synchronous cyclic slip and noise filtering (SCANF) in dual-frequency GNSS-R phase measurements generated by OL tracking. This method can simultaneously handle cyclic slip and noise in OL tracking. At the same time, the performance of this method was demonstrated in the article by using real GNSS-R phase measurement values recorded by the receiver on the Spire low-Earth-orbit (LEO) satellite. The results showed that the average root mean square (RMS) of the sea surface height anomaly (SSHA) obtained by retrieval relative to the MSS was 7.3 cm. OL tracking is a common GNSS-R data processing method that is typically simpler than closed-loop tracking, but also more susceptible to noise and cyclic slip. The experimental results verified the effectiveness and superiority of the method, therefore, the proposal of this method is crucial for improving the effectiveness of OL tracking. In 2022, Li et al. [21] explored the processing of raw IF data from multi-satellite GNSS-R missions and demonstrated the application of raw IF data in inland water detection and elevation measurement, providing new insights for the use of raw IF data in related fields. In addition, in reference [29], the algorithm for detecting surface water in the upcoming HydroGNSS mission was tested using low-speed DDMs from NASA/CYGNSS and raw IF signals collected from CYGNSS and TDS-1. The test results met the 90% accuracy requirement of the mission, demonstrating the importance of studying raw IF data in the design and optimization of spaceborne GNSS-R instruments.

With the continuous improvement and refinement of spaceborne GNSS-R raw IF signal processing technology and related algorithms, the application of spaceborne GNSS-R raw IF signals in inland water bodies, oceans, the ionosphere, the troposphere, and other related fields has great potential and plays a huge role in improving observation accuracy. However, there are still many challenges in the utilization and application of spaceborne GNSS-R raw IF signals, such as the fact that only a few satellites have publicly released raw IF data, the accumulation of raw data is limited, and there is still room for improvement in algorithms and accuracy.

This article focuses on summarizing the current processing status of spaceborne GNSS-R raw IF signals, introducing relevant satellites and some important cutting-edge research fields, including coherent detection and inland water monitoring, sea surface height retrieval, ice height (or ice sheet height) retrieval, ionospheric total electron content and

disturbance observation, and tropospheric monitoring. Although the previous literature has explored certain aspects of this topic, such as land applications [30], these discussions are limited in scope. This article offers a more comprehensive overview, encompassing recent advancements in land, ocean, ionosphere, and troposphere applications of spaceborne GNSS-R raw IF signals. It also highlights the progress made, future prospects, and some existing challenges associated with the use of spaceborne GNSS-R raw IF signals in these domains. This review will provide unique and useful insights into the processing of spaceborne GNSS-R raw IF signals and their various application fields, and also provide some inspiration for researchers who are studying or will study the use of spaceborne GNSS-R raw IF signals for related field applications. The organizational structure of this article is as follows: the second part introduces the current status of spaceborne GNSS-R microsatellites; the third part provides a detailed introduction to coherent detection and inland water monitoring; the fourth part discusses two methods for sea surface height retrieval, including code delay and carrier-phase sea surface height measurement; the fifth part introduces ice cover height; and the sixth and seventh parts respectively discuss total electron content and disturbance observations of the ionosphere, as well as the monitoring of the troposphere. Finally, a summary of the entire article and future prospects for the raw IF signals of spaceborne GNSS-R is presented.

2. Current Status of Spaceborne GNSS-R Microsatellites

Over the past two decades, with the continuous development of science and technology, countries around the world have launched many spaceborne GNSS-R microsatellites. In 2003, the successful launch of the UK-DMC laid the foundation for the development of spaceborne GNSS-R technology [6]. In response to the increasing demand for Earth observation, various countries launched different spaceborne GNSS-R satellite missions in the following years, including the TDS-1 [31], CYGNSS [32], BF-1 A/B [14], FSSCat [12], FengYun-3E/3F/3G [33,34], and Tianmu-1 satellite missions. The successful launch of spaceborne GNSS-R satellite missions has brought new opportunities and promoted the continuous development of spaceborne GNSS-R technology. The development history and specific information of GNSS-R satellite missions are shown in Figure 1 and Table 1.

The satellites currently known to collect raw IF signals among spaceborne GNSS-R satellites mainly include the following, and detailed information about these satellites is provided in reference [21]. Here, we provide a brief introduction to the relevant applications of these satellite raw IF signals.

UK-DMC: This satellite was launched in a sun-synchronous orbit at an altitude of approximately 680 km and has collected multiple sets of raw IF signals [35], from which GPS signals have been discovered [6].

UK-TDS-1: This satellite was launched in low Earth orbit at an altitude of approximately 635 km and an inclination angle of 98.4°. It occasionally collects raw IF samples of direct and reflected signals, which provides opportunities for research on new applications such as sea surface target and sea ice detection [36], sea surface altimetry [37], and ionospheric detection [38], among others.

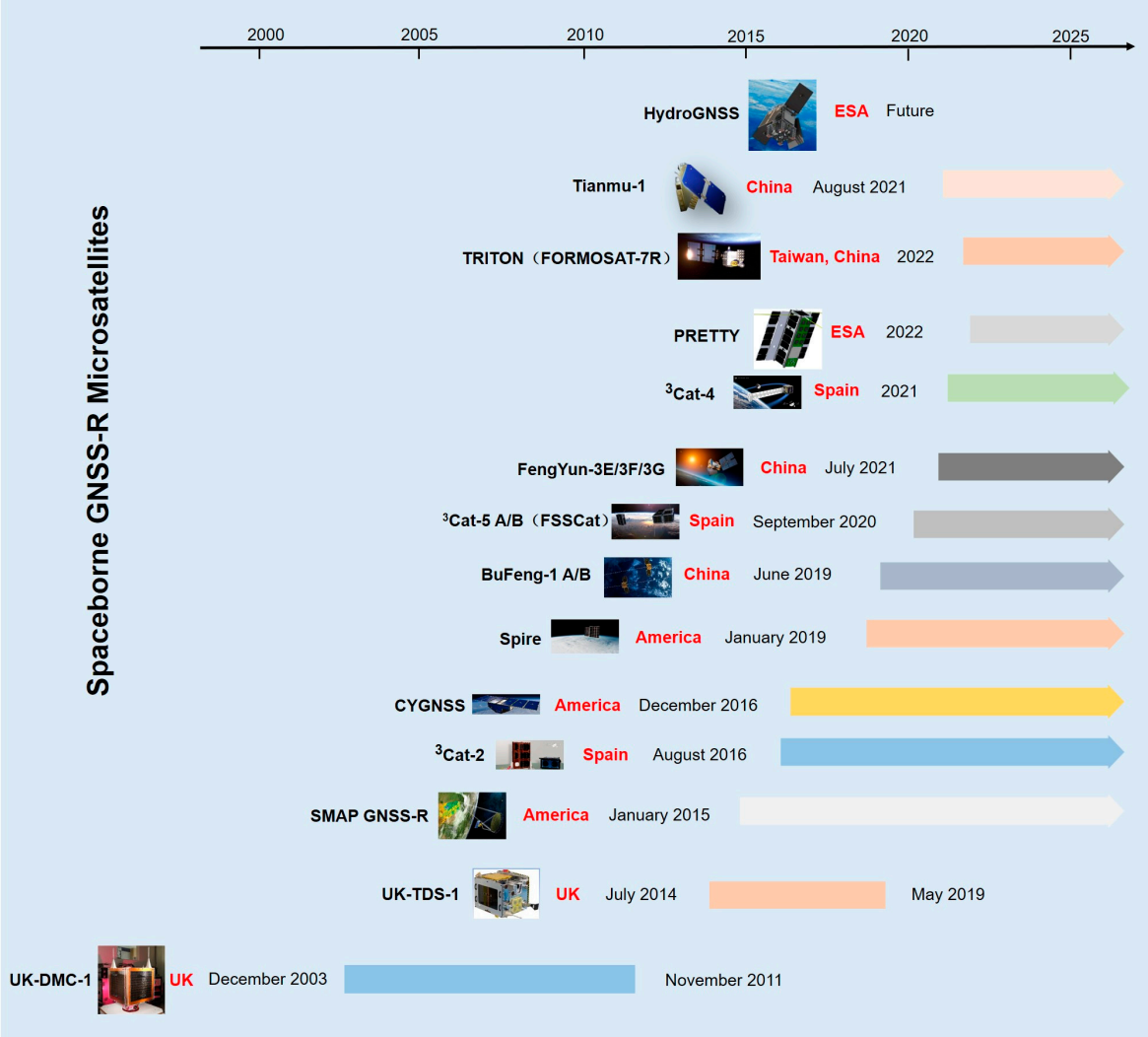


Figure 1. Development history of spaceborne GNSS-R satellite missions https://web.archive.org/web/20070609192647, http://merrbys.co.uk/about/introduction, https://podaac.jpl.nasa.gov/CYGNSS, https://nanosatlab.upc.edu/en/missions-and-projects/3cat-2, https://smap.jpl.nasa.gov/mission/description/, https://earth.esa.int/eogateway/documents/20142/37627/Spire-Product-Guide.pdf, https://satellite.nsmc.org.cn/FY3E/html/index.html, https://nanosatlab.upc.edu/en/missions-and-projects/fsscat; https://space.skyrocket.de/doc_sdat/fsscat.htm, https://nanosatlab.upc.edu/en/missions-and-projects/3cat-4, https://www.esa.int/ESA_Multimedia/Images/2021/09/PRETTY_CubeSat, https://www.esa.int/ESA_Multimedia/Images/2021/03/HydroGNSS, http://www.uux.cn/viewnews94839.html, https://sat.huijiwiki.com/wiki/%E5%A4%A9%E7%9B%AE%E5%8D%AB%E6%98%9F, https://space.skyrocket.de/doc_sdat/musat-1_muon.htm (the rectangle in the figure represents the completed satellite mission, and the arrow represents the satellite mission still in orbit).

CYGNSS: This consists of eight microsatellites launched in low Earth orbit at an altitude of 520 km and an orbital inclination of 35 degrees. Its main task is to measure the sea surface wind speed of tropical cyclones and their surrounding waters [39]. Some studies have processed CYGNSS raw IF signals to generate new CYGNSS data products to improve data resolution and optimize the application of data products in scientific research [40,41]. Currently, CYGNSS raw IF signals are widely used, including in inland water detection [42], inland water height retrieval [24], sea surface height measurement [43], ionospheric detection [44], and the potential of interferometry in height measurement [45].

BuFeng-1 A/B: The BF-1 A/B satellite orbits at an altitude of 579 km, with an orbital inclination of 45° [14]. It occasionally collects raw IF data from the GPS L1 and BDS B1I bands [21], which has been applied in carrier-phase sea surface height measurement [46].

Spire: Spire's GNSS RO satellite is equipped with instruments and antenna configurations capable of receiving reflected signals from GNSS satellites. Specifically, they are able to receive reflected signals from GNSS satellites, which are transmitted in a "grazing angle" (GA) manner. In 2019, Spire launched two new satellites to perform GNSS-R measurements [47]. In addition to business data, some low-level raw IF data are also collected by GNSS-R satellites and applied in fields such as sea ice height retrieval [48] and ionospheric sounding [49].

FY-3E: FY-3E is a near-polar sun-synchronous orbit satellite, successfully launched in 2021, equipped with a GNSS occultation detector (GNOS-II) [34]. It can obtain the raw IF data of a reflected signal within a specific area, but there is no channel to record the raw direct signal. Wang et al. [50] proposed a novel method for tracking individual DDMs without direct or auxiliary data based on GNOS-II to maximize the spatiotemporal resolution of level 1 DDMs.

Among these numerous satellites, most of them only disclose L1 data. Although CYGNSS and TDS-1 provide a small amount of L0-level data, this data has limitations in its distribution range. For example, there is relatively rich data on some land areas, but very little data on the ocean and polar regions, which makes it difficult to meet the research demand for marine and polar scientific research [21]. In addition to CYGNSS and TDS-1 providing a small amount of L0-level data, BF-1 A/B occasionally collects raw IF data in the GPS L1 and BDS B1I frequency bands. It is worth noting that Spire is currently the only satellite that provides dual-frequency L0 data, but the L0 data provided by these two satellites is not publicly available. The GNSS-R receiver carried by China's Tianmu-1 satellites also collect raw IF signals and can simultaneously receive reflection signals from four navigation systems (including BeiDou, GPS, GLONASS, and Galileo) and the Quasi Zenith Satellite System (QZSS). However, the satellites are commercial satellites and these raw data cannot be directly obtained. Although there are currently significant limitations in data acquisition, raw IF signal observation data from satellite missions such as Spire, BF-1 A/B, and Tianmu-1 can be distributed and shared among participating members. Spire and BF-1 A/B have already played a significant role in research in many fields, such as sea surface winds, land surface soil moisture, sea surface height measurements, ionosphere, ice sheet height, and so on [46,51–54]. In the future, with the rapid development of multi-frequency and multi-system GNSS technology and the launch of more spaceborne GNSS-R satellites, there will be more accumulation of raw data, which will be applied in different fields.

Table 1. History of spaceborne GNSS-R microsatellites. ✗ represents L0/L1 level data not publicly available, ✔ represents L0/L1 level data publicly available, and _ represents L0/L1 level data with an uncertain status regarding public availability.

Mission	Type of GNSS-R (Receiver Technique)	Frequency Band/Polarization	GNSS System	Is L0-Level Data Publicly Available?	Is L1-Level Data Publicly Available?
UK-DMC [6]	cGNSS-R	L1/ LHCP	GPS	✗	✗
UK-TDS-1 [31]	cGNSS-R	L1/ LHCP	GPS	✔	✔
CYGNSS [32]	cGNSS-R	L1/ LHCP	GPS	✔	✔

Table 1. *Cont.*

Mission	Type of GNSS-R (Receiver Technique)	Frequency Band/Polarization	GNSS System	Is L0-Level Data Publicly Available?	Is L1-Level Data Publicly Available?
^{3}Cat-2 [55]	cGNSS-R rGNSS-R iGNSS-R	L1/ LHCP, RHCP	GPS GLONASS Galileo BeiDou	✗	✗
SMAP GNSS-R [56]	cGNSS-R	L2/H, V	GPS	✗	✔
BuFeng-1 A/B [14]	cGNSS-R	L1/ LHCP	GPS BeiDou	✗	✗
Spire [52,57–59]	cGNSS-R, GNSS-RO	L1/ LHCP	GPS Galileo	✗	✗
FengYun-3E/3F/3G [33,34]	cGNSS-R, GNSS-RO	L1/ LHCP	GPS Galileo BeiDou	✗	✔
^{3}Cat-5 A/B (FSSCat) [12]	cGNSS-R	L1/ LHCP	GPS Galileo	✗	✗
^{3}Cat-4 [60]	cGNSS-R	L1, L2/ LHCP	GPS Galileo	✗	✗
PRETTY [13,61]	iGNSS-R	L1/ LHCP	GPS Galileo	✗	✗
TRITON (FORMOSAT-7R) [62,63]	cGNSS-R	L1/ LHCP	GPS Galileo QZSS	✗	✗
HydroGNSS [19,64]	cGNSS-R	L1, E1/ LHCP, RHCP	GPS Galileo	–	–
Tianmu-1 [65]	cGNSS-R, GNSS-RO	L1, B1, E1/ LHCP, LHCP + RHCP, H + V	GPS GLONASS Galileo BeiDou QZSS	✗	✗
MuSat Constellation [18]	–	–	–	–	–

3. Coherence Detection and Inland Water Body Monitoring

3.1. Coherence Detection

Coherent GNSS-R signals have great potential in achieving high-precision and high-resolution carrier-phase measurements, playing an important role in altimetry, sea-level monitoring, soil moisture monitoring, flood mapping, and other applications [66]. When defining coherent and noncoherent signals, in general, reflection will exhibit a mixture of coherent and noncoherent components. The effective surface roughness is one of the main factors determining the ratio of coherent and noncoherent power in a given reflection, and the Rayleigh parameter is commonly used to describe the surface condition. The Rayleigh parameter is determined by the root mean square surface height $< \Delta h^2 >^{\frac{1}{2}}$, wavelength λ, and incident angle of reflection θ [67], as follows:

$$R_a = 2\pi \ < \Delta h^2 >^{\frac{1}{2}} \frac{\cos\theta}{\lambda} \quad (1)$$

With an increase in roughness, energy is dispersed outside the specular reflection direction. As the Rayleigh parameter increases, it indicates that the power of coherent reflection from that surface area decreases.

Figure 2 shows the difference between coherent and noncoherent GNSS signal reflections. As shown in the figure, coherent reflection occurs when the reflection surface is sufficiently smooth, while noncoherent reflection occurs when the roughness ε of the reflection surface is equal to or greater than the signal wavelength λ. The Rayleigh criterion provides rough guidance for distinguishing between smooth and rough surfaces with specific wavelengths and elevation angles θ of reflected signals [68], as follows:

$$\varepsilon < \frac{\lambda}{8\sin(\theta)} \tag{2}$$

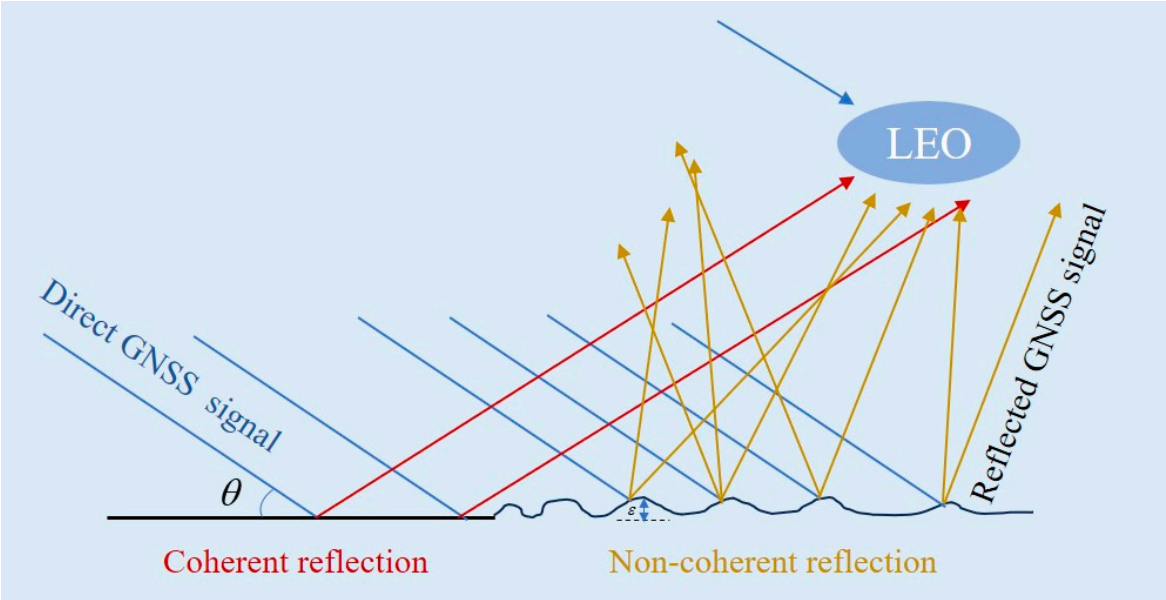


Figure 2. Illustration of coherent and noncoherent GNSS reflection signals [66]. The blue solid line in the figure represents GNSS direct signal, the red solid line represents coherent GNSS reflected signal, and the yellow line represents noncoherent GNSS reflected signal.

Figure 3 shows examples of coherent and noncoherent DDMs observed by different GNSS-R satellites. As shown in the figure, in the FY-3E BDS reflection signal DDM example, Figure 3e,f, DDMs are dominated by coherent signals, while the rest are dominated by noncoherent signals. In the FY-3E GPS reflection signal DDM example, all five subgraphs are dominated by noncoherent signals for DDMs. In the FY-3E GAL reflection signal DDM example, Figure 3d–f, DDMs are dominated by coherent signals, while the rest are dominated by noncoherent signals. In the DDM example for CYGNSS GPS reflection signals, Figure 3a is dominated by coherent signals, while the rest are dominated by noncoherent signals. In the DDM example for TDS-1 GPS reflection signals, all five subplots are dominated by noncoherent signals. Coherent detection plays an important role in high-precision and high-resolution carrier-phase measurement, as carrier-phase measurement can only be performed when reflection is dominated by coherent scattering. In current or future applications of spaceborne GNSS-R, signal coherence is an important condition for high-precision detection. In the application of grazing angle (GA) carrier-phase sea surface height measurement, a centimeter-level height measurement accuracy can be achieved [43]. As early as 2019, Wang and Morton [69,70] found that coherent GPS reflection signals were often observed in the raw IF signals recorded by CYGNSS. They proposed a closed-loop carrier-phase tracking algorithm based on the Kalman filter for tracking coherent GNSS-R signals and processing these coherent reflection signals through open-loop and closed-loop processing, which is of great significance for achieving a centimeter-level height

measurement accuracy. Later, Morton et al. [27] proposed two algorithms for processing low coherent power water reflection signals, namely AHT for low-complexity single-frequency receivers and multi-carrier tracking suitable for wideband front-end hardware. Applying this method to the raw IF signals of CYGNSS can achieve centimeter-level carrier tracking. However, the analysis of tracking data reveals that successful carrier tracking requires a low signal grazing angle, high antenna gain, and low sea surface wind speed.

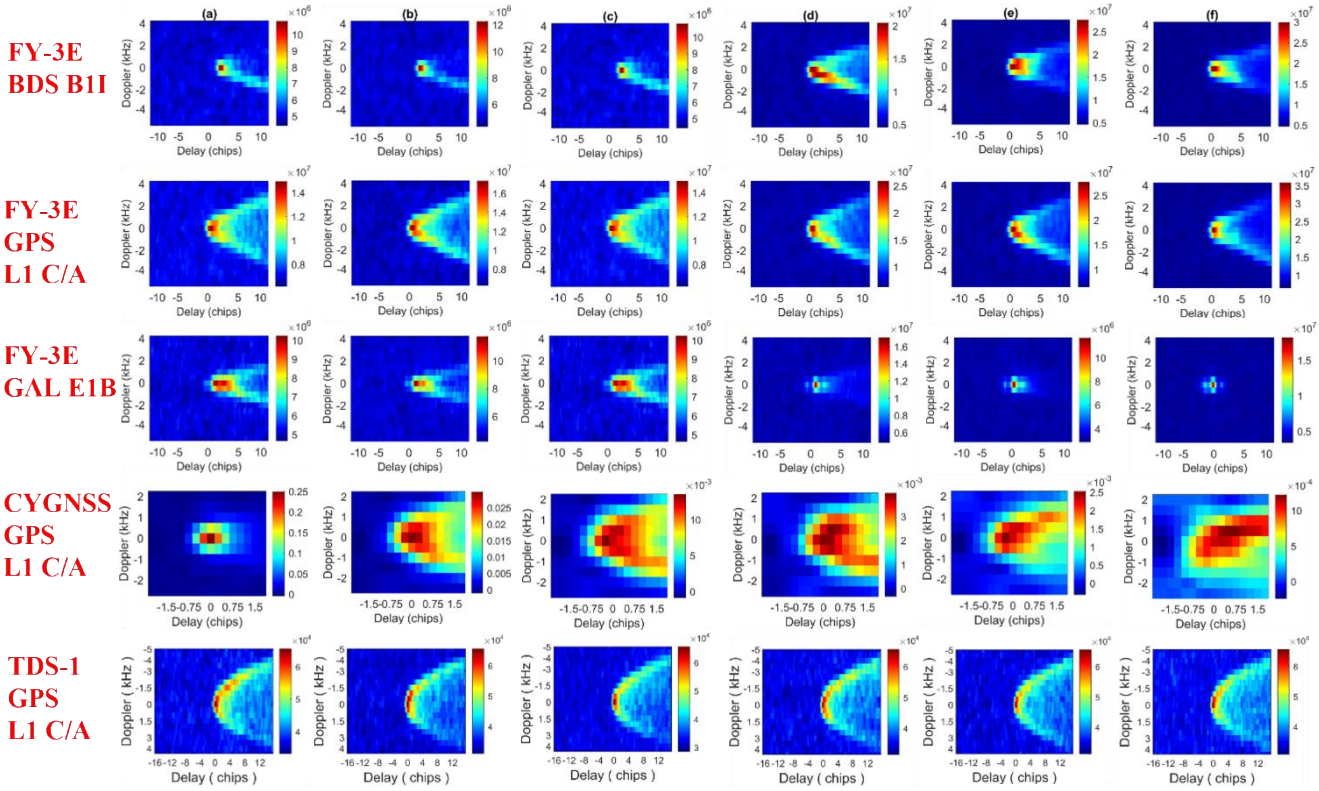


Figure 3. Examples of coherent and noncoherent DDMs observed by different GNSS-R satellites. Each row in the figure represents the DDMs of different GNSS-R satellites; (**a**–**f**) represent DDM under coherent or incoherent dominance.

In recent years, some research has been conducted on the coherent detection of GNSS signal reflections. Figure 4 shows the process flows of three commonly used coherent detection methods using spaceborne GNSS-R raw IF signals, namely cycle statistics (circular length and kurtosis), the signal-to-noise ratio method, and the machine learning method (e.g., SVM). The method based on cycle statistics (circular length and kurtosis) determines whether a signal is coherent or noncoherent according to a preset threshold. The signal-to-noise ratio analysis method distinguishes by calculating the signal-to-noise power ratio of a signal. Machine learning classifies through feature engineering selection, model training, and testing. Roesler et al. [52] proposed a method for the coherent detection of the carrier phase by analyzing Spire Global CubeSat data. OL carrier-phase tracking was used to obtain 50 Hz GPS L1 and L2 carrier-phase estimation data. Two parameters, circular length (CL) and circular kurtosis [71], were applied for coherence detection and quantification. The results showed that this method has potential in ocean and sea ice monitoring. Meanwhile, the study also indicated that when using filtering methods such as SCANF, semi-coherent reflection signals can achieve almost the same accuracy as coherent reflection in retrieving surface height. However, coherence analysis is limited to the hardware and processing software quality of Spire Global CubeSats.

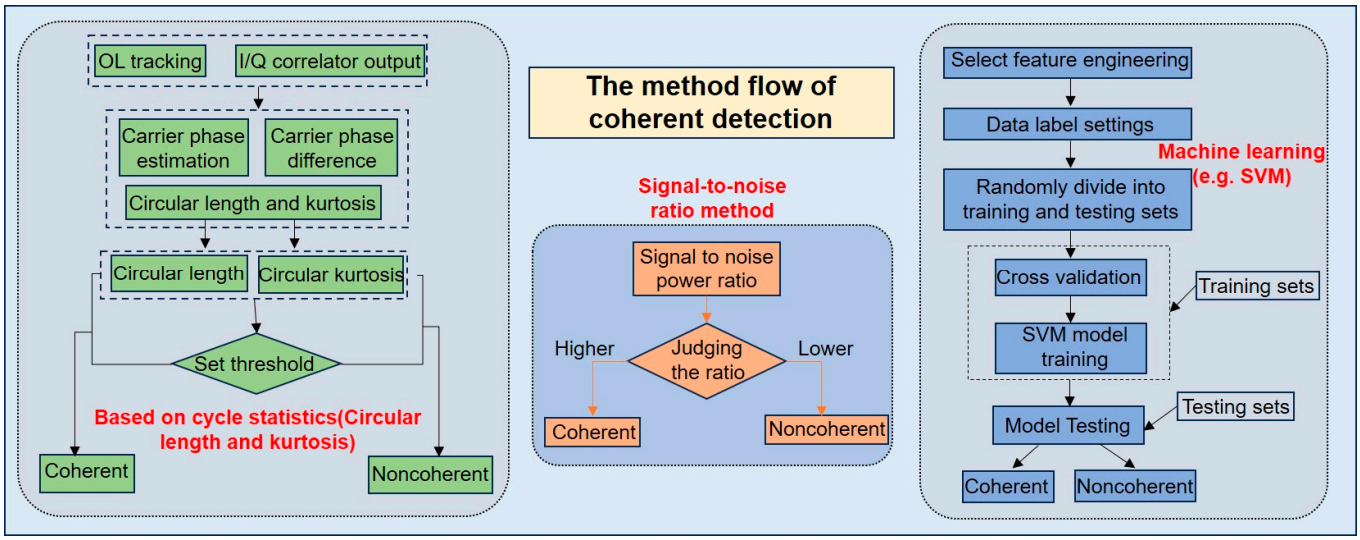


Figure 4. Flow charts of signal coherence detection methods [72,73].

Loria et al. [74] summarized and compared various GNSS-R coherent detection methods. Currently, research on spaceborne GNSS-R coherent detection is mainly based on standard Level 1 DDM products [8,75–79] and raw IF signal data. Among them, the first type of detector based on noncoherent integrated real valued DDM power mainly includes the following three types of detectors: detectors using peak amplitude, detectors using waveform shape, and power spread detectors. The second type of complex DDM based on raw IF signal includes the following three main detectors: a coherence gain detector, phase detector, and entropy detector. Each method has different applicable scenarios and requires different algorithms to be selected according to specific applications, making it difficult to evaluate the advantages and disadvantages. In the second type of coherent detector, amplitude and phase information can be used. Table 2 provides a detailed introduction to the three types of detectors based on complex DDMs generated from raw IF signals [74].

Although there are currently many coherent detection methods for spaceborne GNSS-R, these methods struggle to achieve the coherent detection of signals for multiple scenarios and are quantified in different ways. Based on statistical analysis of the signal-to-noise ratio, circular length, and kurtosis distribution, it is determined that the detection problem is not linearly separable [73]. Among these detection methods, the phase difference circular length method has been widely used, but due to the fact that such detection problems are not linearly separable, the selection of a threshold is not reasonable. This may lead to some good signals being erroneously excluded or some poor signals being erroneously judged as coherent. With the rapid development of computer technology, machine learning has provided new ideas for spaceborne GNSS-R coherent detection. Wang et al. [73] proposed a method for spaceborne GNSS-R coherent detection using Support Vector Machine (SVM), which utilizes the OL tracking data of reflected GPS L1 signals received by Spire LEO satellites, selecting a 50 Hz SNR and carrier-phase error as SVM coherent detection features. The results showed that the method has a detection accuracy of 98.66%. The results of this study provide new ideas and methods for further improving coherent detection algorithms. Machine learning can fully utilize the self-learning and adaptive abilities of brain cells to cope with difficult nonlinear situations. In future research, in order to adapt to such nonlinear problems, it may be necessary to use machine learning and deep learning to solve such nonlinear problems and obtain better detection results.

Table 2. Detailed introduction to three detectors for complex DDMs generated based on raw IF signals.

Detector	Introduce	Related Formulas	Explain
Coherence gain detector [74]	This detector utilizes information from the phase and relative amplitude of the received signal. It distinguishes between coherent and noncoherent signals by comparing the increase in correlated power with a threshold. The longer coherent integration time T_l and the nominal integration time T_n are calculated using the correlated power G_p (in decibels). In addition, to further reduce noise and compare with other coherent detector algorithms, the normalized integrated power values need to be averaged over a longer period of time, and then these average correlated power ratios are normalized by T_l, which we represent as the quantity "coherence" C.	$G_p = 10\log_{10}\frac{T_l}{T_n}$ $C = \frac{T_n}{T_l T_{\text{tot}}} \sum^{T_{\text{tot}}/T_n} \frac{\left\lvert \sum_{i=1}^{T_i/T_n} s_i \right\rvert^2}{\sum_{i=1}^{T_i/T_n} \lvert s_i \rvert^2}$	where T_{tot} is the total signal length and S_i is a sequence of complex samples taken from the DDM after the initial cross-correlation of the measured signal with a local replica. The coherence metric is bounded by [0, 1], where a coherence value of 0 represents a noncoherent signal and a value of 1 represents a fully coherent signal. The typical value of noncoherent reflection is approximately between 0 and 0.2.
Phase detector [52]	This detector is based on phase cycle statistics and coherent detection using the carrier phase, using two parameters, circular length (CL) and circular kurtosis, for coherent detection and quantification [71]. Circular length: average unit vector length of the dataset. Kurtosis: the measurement of the "peak" of an angle dataset:	$\zeta = \frac{1}{N}\left\lvert \sum_{i=1}^{N} \cos a_i + \sum_{i=1}^{N} \sin a_i \right\rvert$ $K = \frac{1}{N}\sum_{i=1}^{N} \cos(2(a_i - \bar{a}_i))$	where $i = 1, 2, 3, \ldots, N$ are uniformly distributed around the unit circle, with values within the range of [0, 1], and $\bar{a}_i$ is the average value of the dataset. If a_i is uniformly distributed around the unit circle, then $\zeta = 1$, $K = 1$. From the above equation, it can be seen that the closer the value of ζ and K is to 1, the more coherent the signal is.
Entropy detector [80]	This detector relies on the generalized eigendecomposition (GED) of the correlation matrix R of complex zero-Doppler delay waveforms. To detect coherence in GNSS-R signals, the concept of von Neumann entropy is used to measure the amount of information contained in generalized eigenvalues.	$\hat{\mathbf{R}} = \frac{1}{N}\mathbf{Z}\mathbf{Z}^H$ $H = -\text{Tr}\left(\frac{\Lambda}{\text{Tr}(\Lambda)}\log\left(\frac{\Lambda}{\text{Tr}(\Lambda)}\right)\right)$	where Z is the $M \times N$ matrix, whose columns are the N, sequential snapshots of the M -length delay waveforms. Λ represents the matrix of normalized eigenvalues, where entropy can effectively represent the dynamic range between eigenvalues related to coherent scattering components and other eigenvalues. In the case of only one strongly coherent component, entropy is 0. On the contrary, only in the case of noncoherent components, the entropy is 1 because there are no major eigenvalues.

The coherence of GNSS-R signals is influenced by various factors, including surface water, soil moisture, terrain, and vegetation. Studies have shown that coherence is most dependent on surface water, but not on terrain or soil moisture [81,82]. The signal-to-noise ratio is also closely related to signal coherence. Therefore, optimizing coherence integration time and selecting appropriate GNSS systems can significantly improve signal quality [83–85]. In addition, it was found that most of the current development of conventional GNSS-R (cGNSS-R) is based on processing GPS L1 C/A signals, and the utilization of modern GNSS signals and the development of future spaceborne GNSS-R payloads are crucial to overcome this limitation. Therefore, in the latest study, Du et al. [86] coherently combined GPS III L1 C/A and L1C signals, which significantly improved the signal-to-noise ratio of the reflected signal. The effectiveness of this method was verified through CYGNSS raw IF data, which can provide a reference for the design of future GNSS-R instruments.

3.2. Inland Water Body Detection

Inland water detection refers to the monitoring and analysis of inland water bodies (such as lakes, rivers, and reservoirs), which is of great significance for maintaining the ecological environment, safeguarding human health, and promoting sustainable development. It also plays an important role in carbon cycling and the global climate [87]. Traditional remote sensing technology is commonly used for tracking inland water bodies, such as the Landsat [88] and Sentinel-2 [89] satellites, which can generate high-resolution images to track inland water bodies. However, optical images are limited by clouds and rain, and cannot be observed during severe weather conditions. Although the synthetic aperture radar (SAR) sensor carried by the Sentinel-1 [89] satellite can perform all-weather and all-day ground imaging under various weather conditions, these two types of sensors cannot detect water bodies under vegetation cover and have a long revisit period.

The emergence of spaceborne GNSS-R technology provides a new method for detecting inland water bodies, as coherent reflections on land mainly occur on relatively calm surface water bodies. Therefore, GNSS-R technology can be used to detect inland water bodies [53]. Previous studies have shown that phase-based coherence (measured by circular length) is more reliable in indicating the presence of water bodies compared to the signal-to-noise ratio, especially when the water surface dominates [90]. In addition, because the amplitude of coherent signals is usually much higher than that of noncoherent ones, very small water bodies can be detected [91]. In previous studies, the potential of spaceborne GNSS-R for dynamic inland water mapping has been demonstrated [79], as well as its ability to detect water bodies under dense vegetation cover [91]. Al-Khaldi et al. [79] analyzed the coherence of the Level 1 DDM product of the CYGNSS constellation to detect inland water bodies. This method detects coherence by judging the different "shapes" of DDMs in coherent and noncoherent scattering regions. Compared with Pekel water cover from Landsat images, its detection accuracy exceeded 80%. Moreover, this result was based on CYGNSS data records of about 2 years, which is significantly shorter than the multi-year datasets relied on by other inland water covers, demonstrating the great potential of spaceborne GNSS-R for mapping inland water bodies. However, the sampling rate of DDMs is usually 1 Hz or 2 Hz and the spatial coverage along the orbit at 1 Hz is about 7 km, which is challenging for applications that require a high spatial resolution. The raw IF data of spaceborne GNSS-R has a high sampling rate. By setting different integration times, the spatial resolution along the orbit can be significantly improved, providing higher-resolution observations [53]. At the same time, studying the raw IF data of spaceborne GNSS-R is of great significance in the design and optimization of spaceborne GNSS-R instruments. In a recent study, Peng et al. [29] tested the algorithm

for detecting surface water in the upcoming HydroGNSS mission by utilizing low-speed DDMs from NASA/CYGNSS and raw IF signals collected from CYGNSS and TDS-1 (with a task accuracy requirement of 90%).

In recent years, some researchers have focused on how to use GNSS-R raw IF data to achieve the accurate detection of inland water bodies. Li et al. [21] demonstrated the application of complex waveforms generated from the CYGNSS FM02 satellite's raw IF dataset for inland water body detection, demonstrating the feasibility and potential of using spaceborne GNSS-R raw IF data in the field of water body detection. In 2021, Li et al. [92] successfully plotted a flood inundation map using the complex DDM generated after processing the raw data collected by CYGNSS for the first time, demonstrating the ability to use complex DDMs for flood inundation mapping. However, the GNSS-R instrument carried by CYGNSS satellites can only cover B1C signals, and it is necessary to focus on the combination of different signal components of BeiDou-3 in the future. In 2022, Zhang et al. [53] introduced a new method for jointly identifying coherent reflections using the carrier phase and reflection signal strength and applied this method to 50 Hz GNSS reflection measurements on the Spire Global Cubesats and CYGNSS satellites to map inland water bodies. By analyzing the reflection signals on the surfaces of water bodies, they successfully plotted the boundaries and extension ranges of these water bodies. However, GNSS reflection is sensitive to the fraction of surface water and may make it difficult to distinguish water bodies that are close to each other. In 2024, a study by Carreno-Luengo et al. [91] showed that it is feasible to detect inland water bodies under dense biomass using raw IF data and L1 data from the CYGNSS satellite, where the raw IF data is used for signal coherence detection. Their work overcame the challenge of detecting water bodies under dense vegetation cover, providing new ideas for the application of spaceborne GNSS-R technology in complex environments. Zhang et al. [42] investigated the effectiveness of using CYGNSS raw IF data for Qinghai Lake boundary detection. By analyzing and processing the CYGNSS raw IF data collected near Qinghai Lake in 2018, higher-delay-resolution and Doppler-resolution DDMs were successfully generated. Compared with the terrain distribution results of Google Earth and global land analysis and discovery, the retrieval results had an error of approximately 0.5 km. This study demonstrates the enormous potential of using spaceborne GNSS-R raw IF data to detect the boundaries of inland water bodies, providing new ideas for monitoring inland water bodies. However, due to the scarcity of data, it is not possible to obtain the complete boundaries of Qinghai Lake. In addition, in a recent study, Mei et al. [93] proposed a method of using CYGNSS raw IF data for multidimensional analysis (including amplitude, time delay, phase, and frequency) to improve water identification ability, in order to address the challenge of limited signal features in distance resolution. This method reduces the distance resolution of water bodies with smaller distances from kilometers to meters, significantly improving the accuracy of inland water detection. Wang and Morton [94] studied the retrieval of river slope based on processing CYGNSS raw IF data. Retrieval was achieved by combining the OL tracking of the reflected signal carrier phase with the application of a new error correction method, demonstrating the potential of using spaceborne GNSS-R to retrieval river slope. Subsequently, Wang and Morton [95] used observation data from the Spire CubeSat to observe the surface gradient of the Mississippi River, confirming that GNSS-R can observe superelevation phenomena, while also observing that L2 signals have higher noise levels under low-ionospheric-gradient conditions. However, if there are steep ionospheric gradients on the signal path, dual-frequency measurements can reduce slope gradient errors. This study provides new insights into the use of GNSS-R phase altimetry for observing relatively narrow rivers. However, compared to previous studies on CYGNSS data, Spire GNSS-R data has higher phase noise.

Table 3 summarizes the key content of the literature on the detection of raw IF signals of spaceborne GNSS-R in inland water bodies. The raw IF data of spaceborne GNSS-R has important application value in inland water detection. At present, the raw IF data of spaceborne GNSS-R is scarce and struggles to meet relevant research needs. However, with the continuous accumulation of spaceborne GNSS-R raw IF data and further in-depth research, it will play an important role in the development of future spaceborne GNSS-R missions. At the same time, spaceborne GNSS-R technology will play an increasingly important role in inland water monitoring, providing strong support for achieving the sustainable utilization of water resources and environmental protection.

3.3. Retrieval of Inland Water Body (Or Lake Water Body) Surface Height

Studying the height measurement of inland water bodies (lake water bodies) plays an important role in water resource management, climate research, ecological environment monitoring, and other fields. The height of inland water bodies (or lake water bodies) can be obtained through missions such as satellite height measurement and radar altimetry [96]. However, the radar altimetry constellation limits the spatiotemporal sampling required for the systematic and periodic mapping of lakes [97]. In GNSS-R, height measurement is based on the differential propagation delay between the direct signal and the reflected signal (known as the bistatic delay), which can be obtained from the ranging code (known as the group delay) or carrier phase (known as the phase delay). The principle of the retrieval of inland water body height is shown in Figure 5.

Table 3. Key content summary of the literature related to inland water body detection.

Reference	Satellite Data	Detection Area	Method	Result (Accuracy)
[91]	CYGNSS L1/L0	Amazon basin, Pantanal wetlands	Entropy detector	Small water bodies can be detected and imaged under heavy vegetation (i.e., 400 tons/hectare).
[42]	CYGNSS L0	Qinghai Lake	Fusion method of signal–power ratio and effective area delay distance (D_{LR})	Can achieve higher spatial resolution (0.7 km), with retrieval result error of about 0.5 km.
[92]	CYGNSS L0	Mississippi River	Coherent Coefficient	Proves the feasibility of using the Beidou-3 signal collected by CYGNSS to map flooding inundation.
[53]	Spire, CYGNSS L0	North America, north Eurasia, and near the Gulf of Mexico (Spire data). Southeast USA, Amazon River basin, and Qinghai–Tibet Plateau (CYGNSS data).	Jointly uses carrier phases and signal strength	As for CYGNSS, the difference is mainly less than 0.43 km, with an average of 0.18 km and a standard deviation of 0.16 km.
[21]	CYGNSS FM02 L0	Rousseau Lake, Florida	Coherent Coefficient	An overlay of the mean coherent coefficient in a Google Earth historical image, which clearly shows the consistency between high coherent coefficient pixels and the presence of inland water bodies.
[93]	CYGNSS L0	Amazon River	The threshold, normalized variance, Z-score, variance, and circular correlation (Cir Cor) discriminations	This multi-feature method achieves a high discrimination accuracy (~90%) and provides a high temporal resolution (20 Hz).
[94]	CYGNSS L0	Orinoco River	OL tracking of the reflection signal phase [71] and a novel error correction approach	The retrieved river surface slope ranges from 3.9 to 5.1 cm/km.
[95]	Spire	Mississippi River	OL tracking	The retrieved river surface slopes range from 2.2 to 16.6 cm/km, with lower sections being flatter.

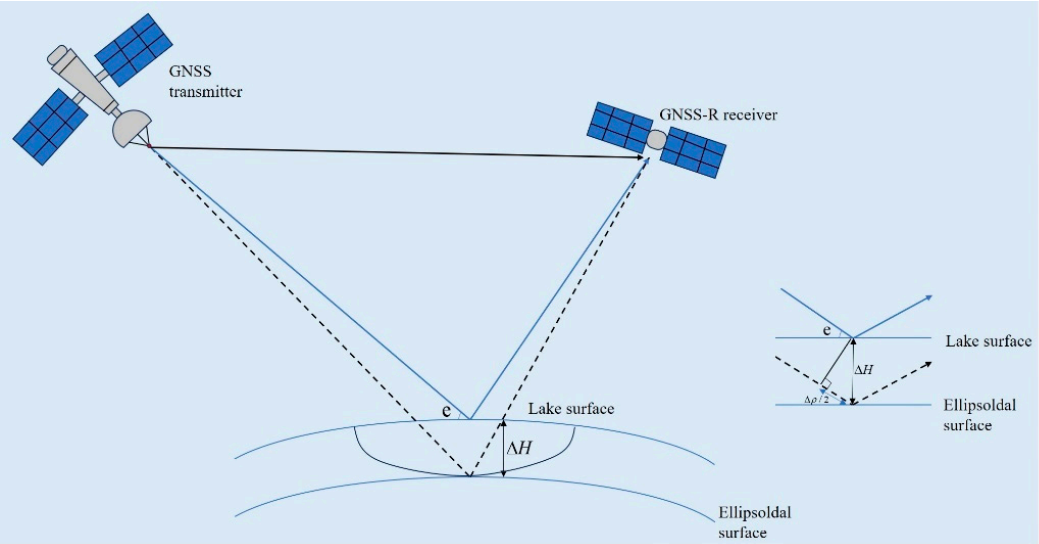


Figure 5. Schematic diagram of retrieval of inland water body height (in this figure, the black dashed line represents the simulated signal on the ellipsoid surface, ΔH is the height of the water surface relative to the ellipsoid surface and e is the satellite elevation angle. Assuming that the observed and simulated reflected signals are parallel to each other, the path difference $\Delta\rho/2$ between the observed and simulated reflected light rays can be represented by ΔH) [98].

In order to perform inland water surface height retrieval, Zhang and Morton [98] used CYGNSS's coherent DDMs from 2020 to 2022 to retrieve the surface height of inland water bodies. They detailed the algorithms and techniques for detecting water surface height using these data, providing a new method for retrieving the height of inland water bodies. However, due to the lack of dual frequency, precise orbit determination, a high waveform delay resolution, and a sufficient calibration capability of instrument delay, CYGNSS has a lower measurement accuracy for inland water body height. In this study, the water surface height ΔH compared to the WGS84 ellipsoid was calculated by the difference between the simulated bistatic delay ρ_m and observed bistatic delay ρ_o, and the satellite elevation angle e at the specular reflection point (SP) was introduced. At the same time, the study further obtained the positive water surface height (water level) by using the EGM2008 geoid undulation [99], and the calculation formula is as follows.

$$\Delta H = \frac{\rho_m - \rho_o}{2 \sin e} \tag{3}$$

$$H = \Delta H - N \tag{4}$$

where N represents the undulation of the geoid relative to the ellipsoidal surface.

Compared to L1 data, the raw IF data of spaceborne GNSS-R has more information, which can be overcome by special processing to overcome the shortcomings of L1 data. At the same time, the carrier phase can provide higher-accuracy measurements. Li et al. [24] demonstrated the use of spaceborne GNSS-R technology to extract the bistatic group delay and carrier-phase delay from quasi specular GNSS reflections using raw IF data from CYGNSS satellites. This study successfully measured the water level and surface topography of the Qinghai Lake as an example. The water level obtained from group delay observation was consistent with Cryosat-2 and in situ measurement results, achieving high-resolution (70 m) and high-precision (centimeter-level) measurements of the lake surface height. This study not only demonstrates the feasibility of using spaceborne GNSS-R raw IF data for water height monitoring, but also provides data support for subsequent research. However, due to receiver orbit errors and ionospheric correction residuals, there

are still errors in group delay height measurements. In this study, the ellipsoidal height H_e of the water surface on the WGS84 ellipsoidal reference surface H_{ref} was calculated by the difference between the simulated bistatic delay ρ_B^m and the observed bistatic delay ρ_B^o, introducing the incident angle i for calculation [2], as follows:

$$H_e = H_{ref} + \frac{\rho_B^m - \rho_B^o}{2\cos i} \quad (5)$$

In 2022, Li et al. [21] demonstrated the application prospects of spaceborne GNSS-R technology in the field of inland water body (lake water body) height retrieval by processing and analyzing the raw IF dataset of multi-task spaceborne GNSS-R, providing important references for subsequent research. Recently, Yanez et al. [97] estimated the lake water level in the Great Lakes region using dual-frequency (GPS L1 and L2) raw grazing angle GNSS-R data provided by the Spire satellite and SAR altimeter data provided by the Sentinel-3 satellite. The results indicated that when using a geoid model with accurate regions, observation accuracy could be improved, and the performance and complementarity of the two data sources in lake water level estimation were evaluated by comparing their results, proving that the comprehensive utilization of these two data sources can improve the accuracy and coverage of lake water level estimation. At the same time, the study pointed out the necessity of improving the geoid model to make these models more sensitive to GNSS-R technology.

The raw IF data of spaceborne GNSS-R has important application value in the retrieval of inland water body height. Carrier-phase measurement can provide a high accuracy and spatial sampling resolution, but the systematic effects of ionospheric correction and orbit determination residuals will also limit phase delay height measurement. In addition, due to the surface roughness driven by wind, it will be difficult to extract coherent phase measurement values from high-altitude satellites (phase information can still be obtained from the grazing angle reflection [100]). In future research, continuous exploration of GNSS-R height analysis under different specular reflection conditions is needed to continuously explore and develop the ability of future GNSS-R missions to monitor global inland water bodies [24].

4. Retrieval of Sea Surface Height

4.1. Code Delay Sea Surface Altimetry

Code delay is an important concept in GNSS positioning systems, which refers to the difference between the signal received by the receiver and the expected arrival time. This difference may be caused by various factors, such as atmospheric delays, receiver and satellite clock errors, and changes in signal propagation paths. Code delay sea surface height measurement is achieved by measuring the round-trip time of signals (i.e., code delay), calculating the distance of the signal propagation, and then estimating the sea surface height. In spaceborne GNSS-R applications, sea surface height measurement is not a specialized task, so the code phase height measurement method based on cross-correlation processing is widely used, with an accuracy of about 9 m [101]. However, using the raw IF signal of spaceborne GNSS-R can obtain results with a higher temporal resolution and trajectory direction spatial resolution [102].

In order to study the delayed sea surface altimetry performance of the raw IF signal code of spaceborne GNSS-R, Li et al. [103] established a marine altimetry accuracy evaluation model in 2018 by analyzing the statistical characteristics of GNSS-R measurement waveforms. The study explored the relationship between height measurement accuracy and waveform statistical characteristics and derived a statistical characteristics analysis model for noncoherent average waveforms. Using the GPS L5 signals obtained on board, a

comparison was made between two delay estimators, based on leading derivative (DER) and waveform fitting (FIT), verifying that the height measurement accuracy of the FIT method was 1.3–1.5 times higher than that of DER. The influence of nonlinear processes (such as square sum noncoherent averaging) on the covariance of complex waveforms was derived, and the covariance model was extended to noncoherent averaging waveforms. Slow-time correlation was analyzed, and the statistical model was validated using airborne SPIR and TDS-1 satellite data, demonstrating a reasonable consistency (within ~10%) between experimental and modeled waveform covariance. The article pointed out that in the parameter space of waveform covariance, it is necessary to consider the influence of significant wave height and non-Gaussian ocean parameters. In future work, it is also necessary to study the waveform statistics of all or partial coherent reflections on smooth surfaces (such as inland water bodies, sea ice, and wetlands) and their impact on height measurement accuracy. In order to consider the influence of more factors in the measurement of sea surface height due to code delay, Mashburn et al. [37] evaluated the performance of spaceborne GNSS-R in ocean altimetry by analyzing the GNSS-R data of TDS-1. The study considered various influencing factors such as orbit, ionospheric, and tropospheric delays and compared them with the average sea surface topography. The results indicated that although the measurement accuracy of 1 s of integration time was limited, the TDS-1 dataset experimentally demonstrated the feasibility of spaceborne GNSS-R height measurement, with a residual surface height of 6.4 m. The study discussed performance-limiting factors and provided recommendations for future GNSS-R altimetry missions for observing mesoscale ocean circulation. Hardware and software performance can be improved to accurately determine and calibrate trajectories. GNSS-R altimetry missions are expected to provide more accurate oceanographic observations in the future. Through hardware and software improvements and precise orbit determination and calibration, future spaceborne GNSS-R missions are expected to provide more accurate oceanographic observations.

In 2019, Li et al. [22] conducted a study using raw data collected from the CYGNSS constellation to conduct an in-depth analysis of the performance of spaceborne GNSS-R technology in ocean altimetry. The reflection waveforms of GPS L1, Galileo E1, and Beidou-3 B1 signals were generated through processing and the delay was estimated using three algorithms, which were converted into sea surface height measurements. Using the raw IF data collected by the CYGNSS satellite and using bistatic geometry [2] to calculate the ellipsoidal height H_e^{obs} of the sea surface above the WGS84 ellipsoid, the following was derived:

$$H_e^{\mathrm{obs}} = -\frac{c\tau_{\mathrm{rtrk}}^{\mathrm{obs}} - (\delta\rho_{\mathrm{iono}} + \delta\rho_{\mathrm{tropo}} + \delta\rho_{\mathrm{b1}})}{2\cos i} \tag{6}$$

where $\tau_{\mathrm{rtrk}}^{\mathrm{obs}}$ is the residual bistatic delay derived from different re-trackers, $\delta\rho_{\mathrm{iono}}$ is the ionospheric delay correction term, $\delta\rho_{\mathrm{tropo}}$ is the two-way slant troposphere delay, $\delta\rho_{bl}$ is the antenna baseline correction, and i is the incident angle. Research has found that the bidirectional ranging accuracy can reach 3.9 m and 2.5 m, but there is a dispersion of inter orbit delay, mainly due to orbit errors of the receiver and ionospheric correction residuals. The study provided important references for the development of GNSS-R ocean altimetry missions and pointed out key considerations for updating CYGNSS mission configurations and future mission development.

Figure 6 shows the process flow of code phase height retrieval, where the phase height retrieval process begins with the coherent processing of the raw IF signal. Firstly, the code phases of the direct and reflected signals are separated, and after denoising and MSS model correction, path delay and orbit error are jointly compensated for. The geometric calculation module synchronously processes L1 observation data, GNSS position, and Sp3 ephemeris, and finally outputs surface elevation through the code phase difference

height measurement method. Song et al. [26] explored the application of spaceborne GNSS-R technology in determining sea-level height based on raw IF data from the TDS-1 satellite, particularly analyzing reflection signals from sea ice and rough sea surfaces. By combining the MSS model and orbit error correction, the accuracy of altitude measurement was improved. The study also found that direct signals may interfere with reflected signals, and attention should be paid to data processing. These achievements provide important references and validation for the application of GNSS-R in the field of ocean altimetry. Faced with the challenges of delayed re-tracking, ionospheric correction, and receiver positioning, Mashburn et al. [104] proposed a delayed re-tracking method based on reflection models, which uses the raw count DDM subtracted from the background noise from the Level 1 data product. Three re-tracking methods (P70, VZ18WAVE and VZ18DDM) were selected from some data in the surrounding waters of Indonesia to retrieve the ocean surface height. The results showed that, without additional time averaging (1 s comprehensive observation from CYGNSS), the VZ18DDM method was superior to the other two methods, and the standard deviations of surface height retrieval based on single-sample and Gaussian smoothing were 5.8 m and 1.9 m, respectively. When averaging for 10 s, the time-averaged results in all cases were significantly better than those achieved with 1 s. At this point, the VZ18DDM method was based on single-sample and Gaussian smoothing with standard deviations of 3.8 m and 1.3 m, respectively. Despite the existence of systematic errors, these methods produced advanced altitude retrieval results, providing important references for the design of future GNSS-R altimetry missions. In the future, the use of GNSS-R instruments and strategies with wider-bandwidth signals and dual-frequency observations is expected to further improve height measurement accuracy and effectively monitor mesoscale ocean topography.

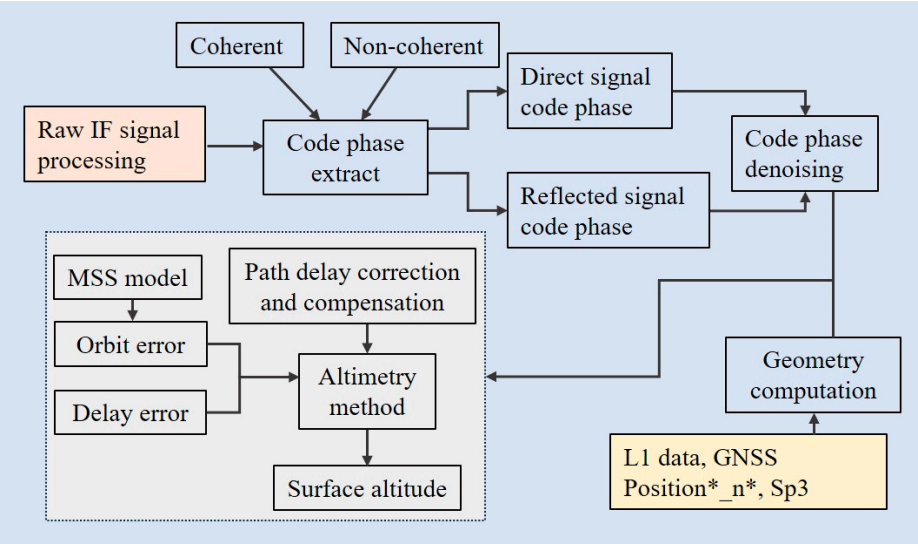


Figure 6. Process flow for phase height retrieval of code [26].

The use of spaceborne GNSS-R raw IF signals in marine surveying still faces challenges such as accurate estimations of signal delay, the correction of atmospheric delay, and orbit errors. In the future, we can focus on using optimized tracking algorithms, applying global ionospheric maps, improving orbit determination accuracy, upgrading hardware and software, and adopting broadband signal and dual-frequency observation technologies to solve these problems.

4.2. Retrieval of Sea Surface Height Using Carrier-Phase Measurement

Carrier-phase delay altimetry, referred to as carrier-phase altimetry (CaPA), measures the phase delay of signals by analyzing the reflection of satellite signals on the sea surface. This technology has been widely used in positioning systems such as GPS and has been implemented on ice sheets [105], sea ice [23,105], and lakes [24]. A change in sea surface height can cause a change in the phase of signal reflection, thus inferring the height information of the sea surface. Unlike code delay height measurement, using spaceborne GNSS-R carrier-phase delay to measure sea surface height can achieve a high-precision measurement of sea surface height (up to the centimeter level). However, there is currently little research on using spaceborne GNSS-R raw IF signals for carrier-phase height measurements of sea surface. The main limitation is that carrier-phase height measurement is limited by the coherence of reflected signals, and the sea surface follows a scattering mechanism. Therefore, this method can only be applied to nearshore and calm sea surface areas, except for observations made under very tilted geometric shapes, as previous studies have shown that very high incident angles can effectively reduce the actual roughness of the sea surface [43,105]. Semmling et al. [106] used carrier waves to observe GNSS signals and established a linear relationship between the Doppler residual values, thereby deriving the deviation of sea surface height and promoting the accuracy of sea surface height retrieval. It has been proposed that observation under very tilted geometric conditions can effectively reduce actual roughness. Semmling et al. [100] obtained GNSS data from a flight at an altitude of 3500 m in the open sea, indicating that in the height measurement results, the elevation angles with centimeter precision for the eight orbits are between 11° and 33°. However, these studies were conducted at low speeds and low altitudes.

In order to evaluate the feasibility of sea surface carrier-phase altimetry for spaceborne GNSS-R, Cardellach et al. [43] first achieved grazing angle carrier-phase sea surface altimetry with a centimeter-level altimetry accuracy. This study used the raw dataset collected by CYGNSS to investigate the accuracy of the system at different frequencies of sampling, achieved through GPS and Galileo signal transmission, and found that the accuracy of the measurement results at 20 Hz downsampling could be compared to professional radar altimeters. But this technology can only be applied under certain relatively calm water surface conditions to obtain sufficient coherence signals for CaPA measurement. Recently, the literature [46] reviewed the BuFeng-1 GNSS-R mission, which used a 20 Hz carrier-phase measurement of sea surface height from BF-1 raw IF samples. The results showed that, compared with DTU MSS products, its evaluation accuracy was in the order of 5 cm. However, elevation angle and sea surface roughness can greatly affect the carrier-phase height measurement of GNSS-R. Studies have shown that carrier-phase height measurement with this accuracy can only be achieved under water surface conditions with wind speeds of less than 6 m/s and waves of less than 1.5 m [43,107]. In addition to using carrier-phase height measurement on the sea surface, recently, spaceborne GNSS-R raw IF data has also been utilized for river slope carrier-phase measurement. River slope is the gradient of river water surface elevation with respect to the geoid. Wang et al. [108] focused on introducing river widths greater than 500 m using CYGNSS and Spire grating-angle GNSS-R raw IF data. Their experimental results showed that on an ideal 5 km river section at a 30° elevation angle, the total uncertainty was approximately 0.38 cm/km. This study demonstrates the potential application of carrier-phase height measurement. Figure 7 shows the flow chart of coherent GNSS-R signal carrier-phase-based altimetry retrieval. Table 4 summarizes the key contents of the two methods for sea surface height retrieval (i.e., code delay and carrier phase) in the relevant literature mentioned above.

Table 4. Summary and introduction of the key contents of two methods for retrieving sea surface height in the relevant literature.

Retrieval Method	Reference	Satellite (Airborne) Data Used	Reference Surface/Data	Result (Accuracy)
Carrier phase	[43]	CYGNSS	DTU18 MSS	The altimetric results show that the measurement system precision is 3/4.1 cm (median/mean) at 20 Hz sampling, cm level at 1 Hz, comparable to dedicated radar altimeters. The combined precision, including systematic errors, is 16/20 cm (median/mean) precision at 50 ms integration (a few cm level at 1 Hz).
Code delay	[104]	CYGNSS	DTU10 MSS	Among the three retracing methods, the VZ18DDM method is the most superior. When averaging for 1 s, the VZ18DDM method is based on single-sample and Gaussian smoothing with standard deviations of 5.8 m and 1.9 m, respectively.
	[37]	TDS-1	DTU10 MSS	Compared to the mean sea surface topography, the surface height residuals are found to be 6.4 m, 1σ with a 1 s integration time.
	[26]	TDS-1	DTU15 MSS	The results show a good consistency with MSS model.
	[103]	SPIR	SPIR, TDS-1	With airborne data, two different delay estimators, based on the DER method and the FIT method, are assessed. By taking the information of the whole leading edge instead of that at the SP, the altimetry precision obtained with the FIT method is proven to be a factor 1.3–1.5 times better than that of DER.
	[22]	CYGNSS	DTU18 MSS	The two-way ranging precision can reach up to 3.9 and 2.5 m with 1 s GPS and Galileo group delay measurement (a factor of ∼2 better for altimetry solution), and its evolution with the signal-to-noise ratio shows good consistency with the theoretical model.

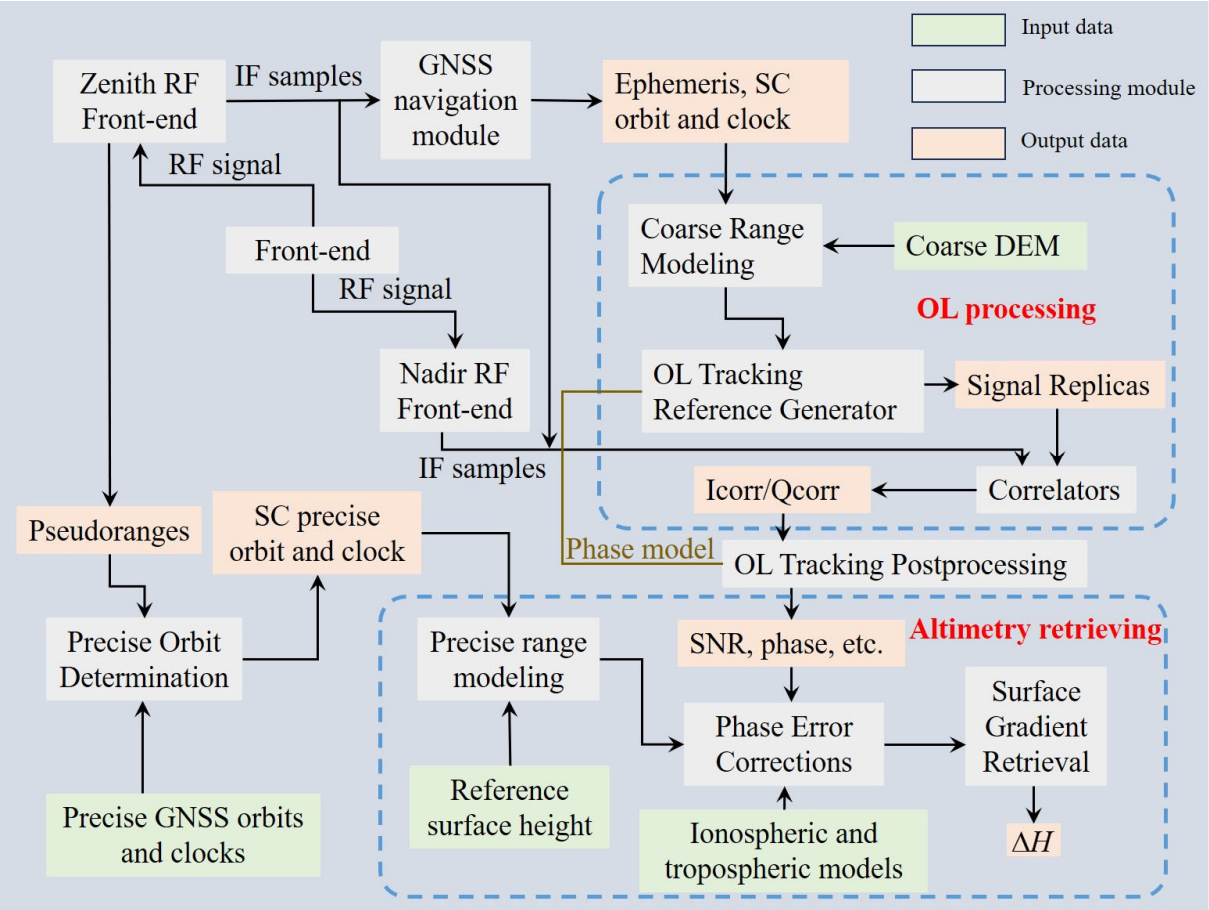


Figure 7. Flow chart of coherent GNSS-R signal carrier-phase-based altimetry retrieval [108].

By utilizing the raw IF data of spaceborne GNSS-R for sea surface carrier-phase height measurement, we can find that carrier-phase measurement is of great help in retrieving high-precision sea surface height. However, there is currently little research on using this technology to retrieve sea surface height. Research on using carrier-phase measurement to retrieve sea surface height still has a long way to go, because the available data is limited and the coherence of reflected signals is affected by the ocean environment. Even under calm sea surface conditions, the availability of data is limited. In the future, the development of spaceborne GNSS-R missions specifically designed to carry out this work is highly likely to study some submesoscale ocean phenomena in different regions of the Earth [43].

5. Ice Height (Or Ice Sheet Height) Retrieval

Ice height refers to the relative height of the ice sheet above the reference ellipsoid, which plays a crucial role in areas such as climate change, ocean resource development, and polar research. Ku band radar (such as Cryosat-2) [107] and laser altimeter (such as ICESat-2) play an important role in measuring sea ice height. In comparison, ICESat-2 can achieve a higher measurement accuracy than Cryosat-2 and can determine the surface height of ice sheets with a higher centimeter-level accuracy. However, orbit satellites with a single base radar or laser systems cannot fill the gaps in conventional repetitive orbits. Using dual-base GNSS-R measurements, data collected from low-Earth-orbit satellites may help to fill these scientific gaps, especially in measurements with small temporal and spatial resolutions [47].

Due to the short wavelength of GNSS carrier signals (∼20–30 cm) and the relatively short chip length of their ranging codes (∼30–300 m), more accurate sea ice height measurements can be obtained using carrier-phase information. Li et al. [23] conducted phase height measurements on sea ice using GNSS-R signals collected by TDS-1 and proposed the sensitivity of satellite GNSS-R carrier-phase observation to changes in sea ice height along the orbit. This study was the first to conduct satellite GNSS-R carrier-phase height measurements on sea ice at a relatively high elevation angle (>57°) under a 20 ms phase delay observation, obtaining a sea ice phase height measurement accuracy with an RMED of 4.7 cm in a 20 ms measurement. However, the lack of TDS-1 orbital position in this study leads to significant orbital errors in time delay measurement, which can have an impact on the retrieval results. Through this study, not only has the feasibility of this technology been verified in sea ice measurement, but it also provides a new method for monitoring sea ice changes and marine environments. In future research, the further analysis and verification of sea ice height retrieval under different thickness and elevation conditions will be conducted based on the availability of TDS-1 and a wider range of raw datasets or complex waveform collection in future spaceborne missions. In 2020, Nguyen et al. [47] extracted height information from the initial grazing angle GNSS reflection event observed by the Spire satellite to determine the application and accuracy of spaceborne GNSS-R technology. The study showed that in areas covered with sea ice, the reflection of GNSS signals exhibited the strongest coherent signal, and the comparison between the estimated surface height at an unsmooth 50 Hz retrieval and the model sea surface showed a good consistency, with an RMS difference of about 3.9 cm. This work marks a preliminary attempt to use this new satellite technology for high-precision surface measurement. By analyzing the phase information of the GNSS signal received by the receiver carried by the Spire satellite, detailed information can be provided about surface features, and a focus on analyzing and studying the influencing factors of height retrieval in future research work is proposed. In 2021, Wang and Morton [48] used coherent GNSS reflection signals recorded by Spire Global Inc.'s LEMUR-2 low-Earth-orbit cube satellite to retrieve sea ice surface

height and evaluated their carrier-phase measurement results. Three examples were used to evaluate the spaceborne GNSS-R sea ice height retrieval. The results showed that the overall trend of the retrieval results was consistent with ICESat-2 measurement results, and the study confirmed that the tropospheric delay model error was the main source of error in GNSS-R sea ice height measurement. In the future, effective methods for correcting tropospheric delay will be studied to improve the accuracy of spaceborne GNSS-R sea ice height measurement.

In order to explore the potential of more spaceborne GNSS-R applications, Li et al. [21] explored the processing methods, data products, and potential applications of raw IF datasets for multi-mission spaceborne GNSS-R. In this study, they demonstrated the potential of spaceborne GNSS-R technology in sea ice height retrieval and monitoring by developing and optimizing processing algorithms. On this basis, Buendía et al. [54] used, for the first time, 17 Spire Global Inc. CubeSat constellations with dual-frequency GNSS-R (GG-R) carrier-phase observation data under grazing geometry to retrieve the ice cover heights in Antarctica and Greenland, and systematically evaluated the retrieval results. The relative heights were adjusted and verified using a Digital Elevation Model (DEM). The study showed that the root mean square error (RMSE) of the two regions, Antarctica and Greenland, was 1.7 m. The GG-R method can supplement the shortcomings of existing satellite altitude measurement products in covering high-latitude areas, providing a promising alternative solution. However, the relatively weak GNSS-R signal and complex bottom morphology at the edges of ice sheets result in low signal coherence, making it difficult for GNSS-R altimetry to sample coastal areas. In future research, it is possible to collect raw IF signals in coastal transition areas and perform relevant processing to solve this problem.

This study uses WGS84 as a reference ellipsoid and calculates the relative height δh above the reference ellipsoid by measuring the difference between the direct signal path TR from the transmitter to the receiver and the distance $T\hat{X}R$ between the reflected signal from the transmitter to the SP and then back to the receiver, without measuring the total ionospheric phase $\Delta\Phi^{RD}_{iono-free}$ and the elevation angle α of the SP. The calculation formula is as follows [54]:

$$\delta h = \frac{T\hat{X}R - TR - \Delta\Phi^{RD}_{iono-fee}}{2sin\alpha} \tag{7}$$

where Δ^{RD} corresponds to the difference between the total phase measurement values of the direct signal and the reflected signal.

Table 5 summarizes the methods for retrieving ice height (or ice sheet height) using spaceborne GNSS-R raw IF signals in the relevant literature, and compares the accuracy of these different methods.

The use of spaceborne GNSS-R raw IF data has shown great development prospects in measuring sea ice height. It is not limited by seasonal and weather conditions and can achieve the continuous monitoring of sea ice throughout the year, providing the possibility for long-term research on sea ice changes. This is of great significance for understanding the seasonal and interannual changes in sea ice. At the same time, it can also provide high-resolution sea ice measurement data to capture small changes in sea ice surface. Spaceborne GNSS-R technology can also be extended beyond the observation range of ICESat-2 and Cryosat-2 to monitor the height of the Antarctic ice sheet, providing valuable data support for high-precision sea ice height measurement. However, spaceborne GNSS-R technology also faces some challenges in measuring sea ice height, especially in the edge areas of ice sheets. Due to low signal coherence, it is difficult to increase the sampling frequency above 50 Hz in coastal areas. In addition, the tropospheric delay model, as the main source of error in sea ice height measurement, will also have a significant impact on the accuracy

of sea ice height measurement. In response to these existing issues, future research can improve GNSS-R measurements by collecting raw IF signals in coastal transition areas. This can increase the number of delay taps and reduce chip spacing, thus better describing the returned waveforms and ultimately evaluating whether it is possible to accurately measure the height of these coastal areas, especially glaciers [54]. In addition, exploring more accurate tropospheric delay correction methods is also an important means to improve the accuracy of sea ice height measurement [48].

Table 5. The methods and accuracy of retrieving ice height (or ice sheet height) in the current published literature.

Reference	Satellite Data Used	Type of Data Used	Reference Surface/Data	Result (Accuracy)
[48]	Spire	L0	ICESat-2	Compared with the monthly average ice freeboard measurement values of ICESat-2 L3B, the GNSS-R retrieval results have a certain consistency with the overall trend of ICESat-2 measurement results.
[47]	Spire	L0	Interpolate from the DTU18 mean sea surface model	The comparison between the unsmooth 50 Hz retrieved surface height estimates and the model sea surface shows a good consistency, with an RMS difference of approximately 3.9 cm.
[54]	Spire	L0	DEM	In Greenland and Antarctica, both the RMSE values retrieved by GG-R and the RMSE values of its reference surface model achieve meter-level accuracy.
[23]	TDS-1	L0	DTU13 MSS	The results show that the RMSD between the measured surface height and the reference one is 4.7 cm with 20 ms phase delay observations (∼140 m along-track sampling distance and ∼400 m spatial resolution).
[21]	TDS-1	L0	DTU13 MSS	The group delay altimetry results show a much larger error comparing to the carrier-phase ones (0.88 m vs. 0.04 m).

6. Ionospheric Total Electron Content and Disturbance Observations

The ionosphere is a part of the Earth's upper atmosphere, located at an altitude from approximately 80 to 1500 km above the Earth's surface. The atoms and molecules within the ionosphere are primarily affected by solar radiation, which ionizes them, forming a weak plasma. This weak plasma influences the refraction and reflection of radio waves, thereby impacting the transmission of wireless signals. For instance, signals from GNSS can experience scattering and diffraction when passing through regions of plasma disturbance or irregularity, leading to fluctuations in signal amplitude and the carrier phase. These effects can cause significant errors in the calculation of position, velocity, and time (PVT) [109]. GNSS is one of the main methods for detecting and simulating parameters such as the total electron content and electron density in the ionosphere [110]. However, the uneven distribution of GNSS ground stations in areas such as oceans and land severely affects the accuracy and reliability of global ionospheric models in these regions. Furthermore, spaceborne GNSS-R has shown great potential in modeling the ionosphere in data-sparse regions [111].

At present, the monitoring of ionospheric total electron content (TEC) and plasma disturbances mainly relies on spaceborne GNSS-R standard data products [98]. In 2016, Camps et al. [112] utilized data from the UK TDS-1 to discover that signal-to-noise ratio fluctuations mainly occur in open-ocean regions and areas of low wind speed within $\pm 20^{\circ}$ of the magnetic equator. The impact of ionospheric scintillation on GNSS reflectometry is similar in both traditional and interferometric techniques. In 2018, Camps et al. [113] focused on the ability of GNSS-R technology to describe ionospheric scintillation characteristics in high- and low-latitude regions. By analyzing GNSS-R ionospheric L1 data

from the Lemur-2 CubeSat payloads of Spire Global Inc. over the past few years, the performance of existing climatological ionospheric scintillation models was assessed, and weaknesses in the models were identified and improved. This provided more accurate data support for satellite communication, Global Navigation Satellite Systems, and Earth observation missions. Considering the effects of tropospheric delay and the ionosphere above spaceborne GNSS-R receivers, Ren et al. [38] proposed an improved method for estimating ionospheric TEC above the ocean, which significantly improved the accuracy of estimating ionospheric TEC.

Despite the progress made in the use of L1 data over the past decades, limitations still exist in terms of spatial resolution, update frequency, and accuracy for current TEC maps. L0 data, on the other hand, offers many advantages. A new method for estimating the slant TEC along the path of reflected signals was proposed in the literature [49], using L0-level data collected from the GNSS-R payloads of the Lemur-2 CubeSat satellites of Spire Global Inc. during 2016 and 2017. The results showed that the TEC data obtained by this method was consistent with existing products and could provide nearly "static" observations of the ionospheric structure, helping to monitor frequent and intense space weather disturbances in polar regions. This method also improved the ability to observe global ionospheric TEC in the presence of coherent GNSS signal reflections over global oceans and inland water bodies, providing a new data source for data-sparse regions. Moreno et al. [114] found that uncertainties in sea surface height were related to ionospheric-model-based group delay altimetry retrieval correction using L0-level data from the Lemur-2 CubeSat satellites of Spire Global Inc., with standard deviations reaching the meter level, demonstrating the great potential of L0-level GNSS-R satellite data for ionospheric research. Wang and Morton [51,115] proposed an innovative application of spaceborne GNSS-R technology in polar ionospheric research using Spire data, providing a new data source that can help to improve ionospheric monitoring and understanding in high-latitude regions.

Ionospheric disturbances significantly affect the propagation of electromagnetic waves. While they have negative impacts on space communication, satellite navigation, and Earth observation technologies, they can also be exploited as a new means of Earth observation. Recent studies have revealed potential associations between seismic activity and ionospheric anomalies [116]. Using GNSS-R technology, positive increments in ionospheric amplitude scintillation in a marine environment were measured, and a small but significant correlation between ionospheric scintillation and earthquake occurrence was explored as a possible precursor to earthquakes [44]. Table 6 summarizes the current methods in the literature for observing ionospheric total electron content and disturbances using spaceborne GNSS-R L1 data and raw IF data, and compares the accuracy of the results for different data types and methods.

This section reviews the current status and potential of GNSS-R technology in measuring ionospheric total electron content and disturbances. Currently, the main method for monitoring the ionosphere is to use GNSS-R standard data products, which have limitations in spatial resolution and update frequency. The use of raw IF data from spaceborne GNSS-R has improved the observation of ionospheric TEC and filled data gaps in oceanic and polar regions. In the future, with the development and application of GNSS-R technology, particularly with the launch of single-frequency GNSS-R missions (such as the ESA's PRETTY mission) and more CubeSats and low-cost satellites, new avenues will be provided for high-resolution global ionospheric observation. These observations will greatly enhance our understanding of the impacts of space weather and geophysical phenomena and provide more reliable data support for satellite communication and navigation systems. Additionally, it is expected that artificial intelligence and machine learning algorithms can be explored to extract more useful information from GNSS-R data, thereby improving

the monitoring and forecasting of ionospheric disturbances. This can provide valuable information for our observations of the ionosphere.

Table 6. Summary of the methods and accuracy of using spaceborne GNSS-R L1 data and raw IF data for ionospheric total electron content and disturbance observations in the current literature.

Reference	Satellite Data Used	Type of Data	Result (Accuracy)
[112]	TDS-1	L1	In low latitudes, open oceans, and low wind speeds, there are coherent scattering components. Under high wind speeds, it is mostly irrelevant.
[113]	TDS-1 CYGNSS	L1	The results show stronger fluctuations in the peak of the DDM associated with ionospheric scintillation events, possibly related to tropical storms.
[44]	CYGNSS	L1	All earthquakes with magnitudes above 4 exhibit a small but detectable positive correlation with ionospheric amplitude scintillation, and the results will improve with increasing magnitudes.
[38]	TDS-1	L1	The improvement in RMS error during high solar activity is 5.3%, and during low solar activity it is 23.5% (compared to GNSS TEC).
[49]	Spire	L0	The slant global ionospheric TEC maps (TEC) retrieved from GNSS-R measurements and GIM follow similar trends, and the TEC time series based on GNSS-R provides an almost "frozen in time" observation of ionospheric structure.
[114]	Spire	L0	The results during the low solar = activity period show that the total tilted electron content fluctuates up to about 300 TECU, the relative ionospheric delay of GPS L1 frequency is 19 m, the Doppler frequency shift is 2 Hz, and the range of peak electron density height variation is from 215 to 330 km.

7. Troposphere Monitoring

The troposphere is the layer of the atmosphere closest to the Earth's surface, with a thickness of 8–18 km, containing a large amount of water vapor, clouds, and aerosols. Water vapor in the troposphere plays a crucial role in global atmospheric radiation, energy balance, and the water cycle, and is an important factor in weather formation and evolution. The wind speed and direction in the troposphere have significant impacts on aircraft. Conducting tropospheric monitoring is of great significance for weather forecasting, disaster prevention and mitigation, climate change research, and ensuring aviation safety. Therefore, conducting tropospheric monitoring and data analysis can deepen our understanding of the Earth's ecosystem and has important scientific significance and practical value in improving climate and weather forecasting.

Total columnar water vapor (TCWV), also known as integrated water vapor (IWV) or total precipitable water vapor, refers to the total amount of water vapor contained in the vertical column of the atmosphere and is a key parameter for studying climate change and meteorological systems. In the past few decades, ground observation, in situ observation, and remote sensing technologies have been commonly used to obtain TCWV, such as satellite observation and reanalysis, radiosondes, microwave radiation measurements, LiDAR, ground Global Navigation Satellite System (GNSS) receiver networks, Very Long Baseline Interferometry (VLBI), and GNSS Radio occultation (GNSS-RO) [117]. However,

due to the various limitations of these technologies (accuracy, spatial density, coverage range, spatial and temporal resolution, cloud coverage, etc.), there is still an urgent need for accurate IWV observations, especially in inland water bodies, oceans, and polar ice scenes.

Tropospheric wet delay (ZWD) is a key parameter for spatial geodesy and meteorological applications, and modeling ZWD is crucial for IWV retrieval and climate monitoring [118]. Currently, ray tracing is one of the most accurate methods for determining ZWD. It is based on a rigorous theoretical foundation and is, therefore, commonly used as a benchmark for ZWD modeling and validation. In addition to ray tracing methods, GNSS has been widely proven to be a unique and powerful tool for estimating ZWD, with advantages such as a high accuracy and high temporal resolution. However, measuring ZWD in harsh environments or locations that are not conducive to setting up stations is challenging, especially in the ocean (due to the uneven distribution of stations, modeling accuracy is inevitably affected), inland water bodies, and polar ice. In addition, various models have been developed to estimate ZWD, including the Hopfield model, the Saatamoinen model, the UNB3 series model, the GPT series model, and the VMF3 model [119,120]. However, these models have some limitations, as it is difficult to accurately estimate the ZWD of low-elevation observations due to the significant spatial and temporal variations in low-level atmospheric humidity. Therefore, ZWD modeling has always been one of the main limiting factors for spatial geodetic observation analysis and application.

Tropospheric delay is an important source of error in GG-R phase height measurement. However, low elevation angles have the opposite effect on the retrieval of surface height and tropospheric delay in GNSS-R. According to the error analysis in reference [28], it is shown that, at an elevation angle of 5°, a total zenith delay (ZTD) of 1 cm in the troposphere, amplified by the tropospheric delay mapping function and phase height retrieval, results in an altitude retrieval error of approximately 65.8 cm. On the contrary, sub-meter-level surface height retrieval deviations (greater than most sea-level model errors) can lead to minor errors in tropospheric delay retrieval at a 5° elevation angle [121]. Due to the uncertainty of humidity delay, the amplification of tropospheric errors in low-elevation GNSS-R provides a valuable opportunity for retrieving atmospheric water vapor content. Wang et al. [28] proposed a ZTD calibration method, which further corrects ZTD errors by fitting altimetry retrieval with MSS and ocean tide models, assuming that the overall trend of the model is accurate over relatively long orbits (such as 300 km). This calibration method significantly improves the root mean square error of height measurement and also proves, for the first time, that the ZTD in the troposphere can be estimated from GG-R. Unfortunately, there is no specific method for ZTD estimation reported in the literature. Jaberi Shafei and Mashhadi-Hossainali [122] first proposed using GNSS reflection signals to solve the rank defect problem in water vapor tomography reconstruction. By optimizing the spatial resolution of the model and implementing an appropriate number of GNSS-R stations, the rank defects of the design matrix were reduced and the reconstruction efficiency was improved. The research results showed that using reflection signal averaging can improve the rank defect of the design matrix by more than 90%, and the average deviation and RMSE of the reconstructed image were 0.2593 and 1.847 ppm, respectively, effectively improving the reconstruction accuracy of the model. Scott et al. [123] introduced the potential and challenges of spaceborne GNSS-R technology in high-precision height measurement applications. The article pointed out that, in order to achieve a centimeter-level ranging accuracy, it is necessary to ensure that the reflected signal can be consistently tracked, which often occurs in low-incident rays. However, at low elevations, tropospheric delay significantly increases, becoming the main source of error in GNSS-R carrier-phase height measurement. A tropospheric error estimation method for low approach angles was proposed to address this issue. Using the Global Pressure and Temperature-3 model, a

comparison was conducted for 328 days at different elevation angles, taking into account the effects under different climate conditions. Research has found that tropospheric errors have significant regional, seasonal, and elevation dependencies, with lower elevations leading to larger error ranges. Considering the GNSS ground reference stations KUUJ and CPNM located in Hudson Bay and the Java Sea, respectively, at an elevation of 45 degrees, the monthly average tropospheric error range of the KUUJ station ranges from −6.8 cm to 5.4 cm and that of the CPNM station ranges from −18.4 cm to 20 cm. When the elevation angle drops to five degrees, the range of tropospheric errors significantly increases, with the KUUJ station ranging from −46.7 cm to 38.3 cm and the CPNM station ranging from −143.3 cm to 146.3 cm. Moreno et al. [124] studied the possibility of ZTD retrieval using airborne coherent GNSS reflection measurement data observed in coastal waters. By obtaining residual phase observations, a 0.5 Hz empirical Doppler extended threshold was established to extract coherent reflections. The results indicated that coherent observations respond well to very calm water bodies and low elevation angles, with a deviation of 5% in estimating ZTD for airborne coherent GNSS-R at low elevation angles (10°). Although this study demonstrated, for the first time, the enormous potential of airborne GNSS-R coherent phase observations in ZTD retrieval, existing technologies face challenges in obtaining high-precision, high spatiotemporal resolution ZTD information for most coherent reflection areas such as oceans, polar sea ice, and inland water bodies. Furthermore, no method for retrieving ZWD and(or) IWV has been proposed.

In order to achieve high-precision, high-spatial-resolution, and high-temporal-resolution TCWV monitoring, in 2023, Wang [121,125] explored a new method for retrieving tropospheric delay and TCWV from GNSS-R using Spire CubeSats data for the first time. The flowchart of this method is shown in Figure 8. The comparison between IWV retrieval using Spire GG-R and ERA5 products, as well as the measurement of IWV data using Sentinel-3 land and sea colorimeter (OLCI), showed a good performance. Among them, the GNSS-R tilted tropospheric delay is estimated to be as follows:

$$\hat{T}_R(t) = \hat{\Phi}_R(t) - \hat{g}_R(t) - \hat{I}_R(t) + M(t)\lambda + \epsilon(t) \tag{8}$$

where $\hat{\Phi}_R$ represents the phase range of the reflected signal, $\hat{g}_R$ and $\hat{I}_R$ represent the geometric and clock components respectively, M represents another unknown integer for phase ambiguity, and ϵ represents the influence of various estimation errors and noise.

The tilted tropospheric delay can be modeled as follows:

$$T_R(t) = 2 \times \left(ZHD(t) \times m_{dry}(\theta(t)) + ZWD(t) \times m_{wet}(\theta(t)) \right) \tag{9}$$

where m_{dry} and m_{wet} are the mapping functions of zenith rest delay (ZHD) and zenith wet delay (ZWD), respectively.

The estimated ZWD value can be converted to TCWV using the following formula:

$$TCWV = \Pi \times ZWD \tag{10}$$

where Π is the conversion factor in units of $kg \cdot m^{-2} \cdot mm^{-1}$.

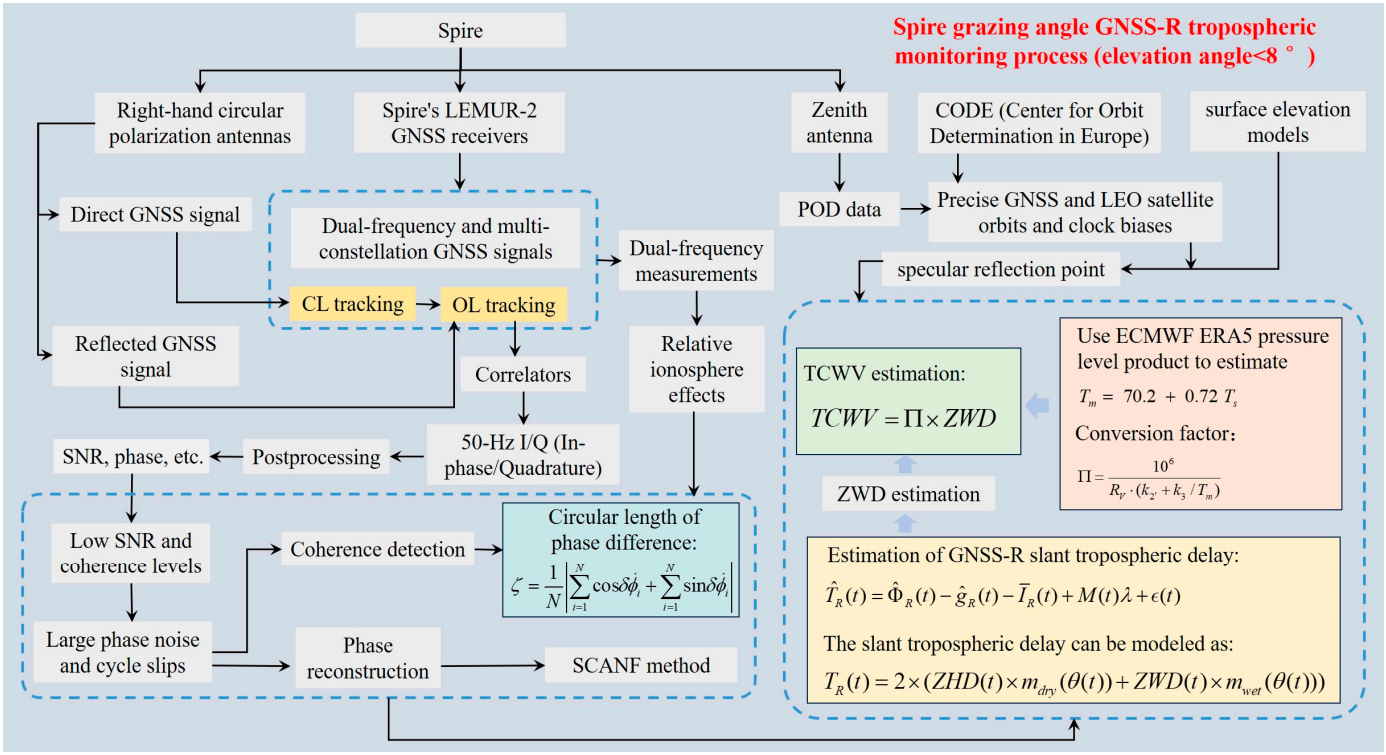


Figure 8. Flow chart of tropospheric monitoring (for relatively smooth ocean and ice surfaces) [121].

Due to the current lack of high-spatial-resolution ocean sky observation methods with short revisit periods, it is difficult to accurately capture the dynamic changes of IWVs. The use of low-cost cube satellites in low Earth orbits has great potential, providing near-high-resolution insights into IWV changes in tropical oceans and valuable data for climate monitoring and atmospheric research. In the latest study, Roesler and Morton [126] used Spire Global grazing angle GNSS-R data collected in low-altitude areas ranging from 5° to 8° in 2022 to achieve accurate calculations of IWVs. However, so far, only a few studies have conducted preliminary studies on IWV retrieval using Spire satellite dual-frequency GPS-R Raw IF signal observation data. There is no research in the literature on the retrieval of ZWD and IWV for inland water bodies or (and) Antarctic scenes, nor is there any report on the specific methods and experimental results of using single-frequency Multi GNSS (GPS, Galileo, and BeiDou-3) raw IF signal data from the TDS-1 and CYGNSS satellites to retrieve ZWD and/or IWV, let alone the results of using Galileo and BeiDou-3 reflection signals to retrieve ZWD and IWV. The analysis in [22] indicated that the waveform front of Galileo E1 B/C and BeiDou-3 B1C signals was much steeper than that of GPS L1 C/A signals, which means that the ranging sensitivity is better and is expected to play an important role in high-precision ranging applications of GNSS reflected coherent signals. There are limitations in the use of dual-frequency GPS raw IF reflection signal observation data in the current Spire constellation, which seriously hinder researchers from further innovating and developing the cutting-edge topic of GG-R ZWD and IWV retrieval.

Spire CubeSats is a small satellite network deployed by Spire, which collects and analyzes Earth observation data in real time through advanced sensors and communication equipment, covering fields such as meteorology, oceanography, and navigation. It also provides global positioning and tracking services, providing data support and solutions for industries such as aviation and navigation. Through case studies, it has been proven that this method can achieve the high-precision detection of tropospheric delay and water vapor in oceans and ice. Then, Spire grazing angle GNSS-R data can be utilized. It was

found that under appropriate conditions, both the ocean surface and sea ice can reflect coherent GNSS signals. Compared with other satellite observation technologies, grazing angle GNSS-R can fill some gaps in atmospheric water vapor observation data. However, research has also pointed out the relative oblique tropospheric delay and elevation-related errors in GNSS-R carrier-phase measurement, and called for future work to strengthen error quantification and improve measurement methods. In addition, research suggests that this method complements GNSS RO, but also suggests the possibility of further utilizing low-elevation reflection signals. Therefore, future research should explore this field more comprehensively to promote the further development and application of this method.

These studies used L0-level data, so we can conclude that applications based on spaceborne GNSS-R raw IF signals have shown unique advantages in monitoring tropospheric water vapor. By capturing the IF signal of GNSS, the propagation characteristics of the signal and its changes as it passes through the troposphere can be analyzed in detail. These signals exhibit different delay and attenuation characteristics during reflection and direct reflection due to different water vapor contents in the troposphere. By accurately measuring and analyzing these characteristics, researchers can estimate the water vapor content in the troposphere, providing a new source of data for meteorological forecasting and climate research. However, although this technology has made some progress, it still faces some challenges. Problems such as modeling errors in the troposphere and elevation-related errors still need to be addressed. Future research should strengthen error quantification and improve measurement methods, while exploring the possibility of complementing GNSS RO and further utilizing low-elevation reflection signals. The TDS-1 and CYGNSS satellites launched by the UK and the US in July 2014 and December 2016, respectively, collected single-frequency Multi GNSS (GPS, Galileo, and BeiDou-3) raw IF signal data reflected from some land, inland water bodies, oceans, and polar sea ice on a global scale. These data were made available to the public for free, providing new opportunities for researchers to use spaceborne GG-R technology to retrieve the ZWD and IWV of inland water bodies, oceans, and polar sea ice regions, in order to expand and promote the innovative application of spaceborne GG-R technology in tropospheric remote sensing. Therefore, it is necessary to use the single-frequency Multi GNSS (GPS, Galileo, and BeiDou-3) reflected raw IF signals from the CYGNSS/TDS-1 satellite in the future to study the retrieval of ZWD and IWV in inland water bodies, oceans, and polar regions, which has important scientific significance and application value. It is worth mentioning that the current BuFeng-1 A/B and Tianmu-1 satellite constellations also collect multi-system GNSS-R raw IF signals [46]. Fortunately, the observation data of Tianmu-1 multi-system spaceborne GNSS-R raw IF signals have also been authorized and provided to the research team members where the author of this paper is located, which will help in ZWD and IWV retrieval in inland water bodies, oceans, and polar sea ice regions. These efforts will promote the wider application of this technology in marine environmental research and climate monitoring and enhance its practical value in weather forecasting, disaster prevention and mitigation, and aviation safety.

8. Summary and Future Prospects

The raw IF signals in spaceborne GNSS-R has broad application prospects. This article summarizes the application status of this technology in multiple fields, including the launch status of spaceborne GNSS-R microsatellites, coherence detection, inland water detection, the surface height measurement of inland (or lake) water bodies, group delay sea surface height measurement, carrier-phase sea surface height measurement, ice height (or ice sheet height) retrieval, ionospheric total electron content and disturbance observations, and troposphere monitoring. These application studies demonstrate enormous potential in multiple fields for GNSS-R raw IF signal measurement technology. In addition to the

applications in various fields mentioned above, researchers are also constantly exploring other applications. In the latest study, Anderson et al. [127] proposed a new GNSS-R cryosphere application, which proves the practicality of spaceborne GNSS-R in the remote sensing of ice shelf surface deformation and roughness. However, the raw IF signals of spaceborne GNSS-R are still in the early stages of research, and L1 data is still dominant in various fields of application. Compared with L1 data, raw IF data contains more information, which provides new ideas for our research. As early as 2022, in the study by Li et al. [22], it was mentioned that the Institute of Space Sciences (ICE-CSIC, IEEC) generated corresponding data products from raw IF datasets collected by different missions. The raw IF datasets collected by TDS-1, CYGNSS, BF-1 A/B, and SPIRE RO missions can be accessed by the ICE-CSIC/IEEC team. These data products are publicly available through a public open-data server to promote new research and explore the potential of GNSS-R in new geophysical applications and future satellite missions. However, so far, the number of satellites that can provide raw IF data for spaceborne GNSS-R is limited, and it is not possible to provide sufficient raw data sets for application in various fields of research. In the future, with the launch of more spaceborne GNSS-R satellites and the accumulation of more raw data, raw IF data will be applied in different fields and can provide higher-accuracy measurement results. Therefore, with the continuous development and improvement of technology, the future should focus on the following aspects.

The accuracy of signal processing and reflection signal analysis should be further improved. Future research should focus on developing more advanced algorithms and technologies to improve the efficiency of signal processing and the accuracy of reflection signal analysis. The integration and collaborative application of other remote sensing technologies should be strengthened. Spaceborne GNSS-R can be combined with other remote sensing technologies, such as radar and optical remote sensing, to achieve multi-source data fusion and improve the comprehensiveness and diversity of Earth observations. Application areas should be expanded, especially in environmental monitoring, climate change research, and weather prediction. The high spatiotemporal resolution and global coverage of spaceborne GNSS-R give it enormous potential in these fields, and future research should focus on applications in these key areas. The commercialization and engineering development of spaceborne GNSS-R technology should be promoted. Applying technology to practical applications requires overcoming a series of engineering and commercialization challenges, including data processing, data transmission, and data application. With the development of GNSS, more GNSS satellites and civilian signals can be used for GNSS-R. The development of new spaceborne processing strategies can improve the observational performance of spaceborne GNSS-R. In the latest study, Du et al. [86] proposed a spaceborne GNSS-R signal processing method that significantly improves the signal-to-noise ratio of reflected signals by coherently combining GPS III L1C/A and L1C reflection signals. This method has been validated using CYGNSS raw IF data, and the results show that compared with the L1C/A waveform, the signal-to-noise ratio of the combined reflection waveform can be improved by about 2 dB. In experiments on height measurement and wind speed measurement, the combined reflection measurement results showed a significant improvement in measurement accuracy compared to L1C/A. This study provides us with new research ideas. Therefore, the new GNSS-R spaceborne signal processing method can provide a reference for the design of future GNSS-R instruments. In the future, we should also explore and process various types of spaceborne GNSS-R reflection signals, improve the design of GNSS-R instruments, and continuously improve the quality of spaceborne GNSS-R signals to achieve higher-accuracy measurement results.

Author Contributions: All authors have made significant contributions to this manuscript. Conceptualization, J.B.; validation, J.B. and Q.W.; formal analysis, Q.W., Y.W., D.H. and H.Y.; writing—original

draft preparation, Q.W., Y.W. and D.H.; writing—review and editing, J.B., Q.W., Y.W. and X.Z.; supervision, J.B.; funding acquisition, J.B. and X.Z. All authors have read and agreed to the published version of the manuscript.

Funding: This work was supported in part by the National Natural Science Foundation of China under Grants 42404037 and 42471483, in part by the Yunnan Fundamental Research Projects under Grant 202401CF070151, in part by the Platform Construction Project of High-level Talent in Kunming University of Science and Technology under Grant 20230041, in part by the National College Students' Innovation and Entrepreneurship Training Program, under Grant 202410674088; in part by the Student Extracurricular Academic and Technological Innovation Fund of Kunming University of Science and Technology, under Grant 2024ZK091; and in part by the Innovative Training Plan Program for College Students of Yunnan Province, under Grant S202310674221.

Data Availability Statement: The GNSS-R data of FY-3E can be obtained from the Fengyun Data Service Network, the URL is https://satellite.nsmc.org.cn/portalsite/default.aspx, accessed on 12 March 2025; The CYGNSS data presented in this study are openly available in PO.DAAC at https://cygnss.engin.umich.edu/data-products/, accessed on 12 March 2025. The spaceborne GNSS-R data from TDS-1 mission is available at www.merrbys.co.uk, accessed on 12 March 2025.

Acknowledgments: We would like to thank NASA for providing CYGNSS data and the TDS-1 and CYGNSS scientific teams for their hard work in providing the data used in this study. The authors would like to thank the anonymous reviewers for their in-depth reviews and helpful suggestions that have largely contributed to improving this article.

Conflicts of Interest: The authors declare no conflicts of interest.

References

1. Hall, C.D.; Cordey, R.A. Multistatic Scatterometry. In Proceedings of the International Geoscience and Remote Sensing Symposium, Remote Sensing: Moving Toward the 21st Century, Edinburgh, UK, 12–16 September 1988; pp. 561–562.
2. Martín-Neira, M. A pasive reflectometry and interferometry system (PARIS) application to ocean altimetry. *ESA J.* **1993**, *17*, 331–355.
3. Martin-Neira, M.; Caparrini, M.; Font-Rossello, J.; Lannelongue, S.; Vallmitjana, C.S. The PARIS concept: An experimental demonstration of sea surface altimetry using GPS reflected signals. *IEEE Trans. Geosci. Remote Sens.* **2001**, *39*, 142–150. [CrossRef]
4. Cardellach, E.; Fabra, F.; Nogués-Correig, O.; Oliveras, S.; Ribó, S.; Rius, A. GNSS-R ground-based and airborne campaigns for ocean, land, ice, and snow techniques: Application to the GOLD-RTR data sets. *Radio Sci.* **2011**, *46*, 1–16. [CrossRef]
5. Balasubramaniam, R.; Ruf, C. Characterization of rain impact on L-Band GNSS-R ocean surface measurements. *Remote Sens. Environ.* **2020**, *239*, 111607. [CrossRef]
6. Gleason, S.; Hodgart, S.; Yiping, S.; Gommenginger, C.; Mackin, S.; Adjrad, M.; Unwin, M. Detection and Processing of bistatically reflected GPS signals from low Earth orbit for the purpose of ocean remote sensing. *IEEE Trans. Geosci. Remote Sens.* **2005**, *43*, 1229–1241. [CrossRef]
7. Zhang, Y.; Huang, S.; Han, Y.; Yang, S.; Hong, Z.; Ma, D.; Meng, W. Machine Learning Methods for Spaceborne GNSS-R Sea Surface Height Measurement From TDS-1. *IEEE J. Sel. Top. Appl. Earth Obs. Remote Sens.* **2022**, *15*, 1079–1088. [CrossRef]
8. Alonso-Arroyo, A.; Zavorotny, V.U.; Camps, A. Sea Ice Detection Using U.K. TDS-1 GNSS-R Data. *IEEE Trans. Geosci. Remote Sens.* **2017**, *55*, 4989–5001. [CrossRef]
9. Rius, A.; Cardellach, E.; Fabra, F.; Li, W.; Ribó, S.; Hernández-Pajares, M. Feasibility of GNSS-R Ice Sheet Altimetry in Greenland Using TDS-1. *Remote Sens.* **2017**, *9*, 742. [CrossRef]
10. Rautiainen, K.; Comite, D.; Cohen, J.; Cardellach, E.; Unwin, M.; Pierdicca, N. Freeze–Thaw Detection Over High-Latitude Regions by Means of GNSS-R Data. *IEEE Trans. Geosci. Remote Sens.* **2022**, *60*, 4302713. [CrossRef]
11. Ruf, C.; Gleason, S.; Ridley, A.; Rose, R.; Scherrer, J. The nasa cygnss mission: Overview and status update. In Proceedings of the 2017 IEEE International Geoscience and Remote Sensing Symposium (IGARSS), Fort Worth, TX, USA, 23–28 July 2017; pp. 2641–2643.
12. Camps, A.; Golkar, A.; Gutierrez, A.; Azua, J.A.R.d.; Munoz-Martin, J.F.; Fernandez, L.; Diez, C.; Aguilella, A.; Briatore, S.; Akhtyamov, R.; et al. Fsscat, the 2017 Copernicus Masters' "Esa Sentinel Small Satellite Challenge" Winner: A Federated Polar and Soil Moisture Tandem Mission Based on 6U Cubesats. In Proceedings of the IGARSS 2018—2018 IEEE International Geoscience and Remote Sensing Symposium, Valencia, Spain, 22–27 July 2018; pp. 8285–8287.

13. Dielacher, A.; Fragner, H.; Koudelka, O.; Beck, P.; Wickert, J.; Cardellach, E.; Høeg, P. The ESA Passive Reflectometry and Dosimetry (Pretty) Mission. In Proceedings of the IGARSS 2019—2019 IEEE International Geoscience and Remote Sensing Symposium, Yokohama, Japan, 28 July–2 August 2019; pp. 5173–5176.
14. Jing, C.; Niu, X.; Duan, C.; Lu, F.; Di, G.; Yang, X. Sea Surface Wind Speed Retrieval from the First Chinese GNSS-R Mission: Technique and Preliminary Results. *Remote Sens.* **2019**, *11*, 3013. [CrossRef]
15. Huang, F.; Xia, J.; Yin, C.; Zhai, X.; Xu, N.; Yang, G.; Bai, W.; Sun, Y.; Du, Q.; Liao, M.; et al. Assessment of FY-3E GNOS-II GNSS-R Global Wind Product. *IEEE J. Sel. Top. Appl. Earth Obs. Remote Sens.* **2022**, *15*, 7899–7912. [CrossRef]
16. Bu, J.; Wang, Q.; Wang, Z.; Fan, S.; Liu, X.; Zuo, X. Land Remote Sensing Applications Using Spaceborne GNSS Reflectometry: A Comprehensive Overview. *IEEE J. Sel. Top. Appl. Earth Obs. Remote Sens.* **2024**, *17*, 12811–12841. [CrossRef]
17. Fu, N.; Li, F. An Introduction of GNSS Reflectometer Remote Sensing Mission From Yunyao Aerospace Technology Co, Ltd. In Proceedings of the 2021 IEEE Specialist Meeting on Reflectometry using GNSS and other Signals of Opportunity (GNSS+R), Beijing, China, 14–17 September 2021; pp. 77–81.
18. Roberts, M.; Colwell, I.; Chew, C.C.; Masters, D.; Nordstrom, K. The Muon Space GNSS-R Surface Soil Moisture Product. *arXiv* **2024**, arXiv:2412.00072.
19. Unwin, M.J.; Pierdicca, N.; Cardellach, E.; Rautiainen, K.; Foti, G.; Blunt, P.; Guerriero, L.; Santi, E.; Tossaint, M. An Introduction to the HydroGNSS GNSS Reflectometry Remote Sensing Mission. *IEEE J. Sel. Top. Appl. Earth Observ. Remote Sens.* **2021**, *14*, 6987–6999. [CrossRef]
20. Bu, J.; Liu, X.; Wang, Q.; Li, L.; Zuo, X.; Yu, K.; Huang, W. Ocean Remote Sensing Using Spaceborne GNSS-Reflectometry: A Review. *IEEE J. Sel. Top. Appl. Earth Obs. Remote Sens.* **2024**, *17*, 13047–13076. [CrossRef]
21. Li, W.; Cardellach, E.; Ribó, S.; Oliveras, S.; Rius, A. Exploration of Multi-Mission Spaceborne GNSS-R Raw IF Data Sets: Processing, Data Products and Potential Applications. *Remote Sens.* **2022**, *14*, 1344. [CrossRef]
22. Li, W.; Cardellach, E.; Fabra, F.; Ribo, S.; Rius, A. Assessment of Spaceborne GNSS-R Ocean Altimetry Performance Using CYGNSS Mission Raw Data. *IEEE Trans. Geosci. Remote Sens.* **2020**, *58*, 238–250. [CrossRef]
23. Li, W.; Cardellach, E.; Fabra, F.; Rius, A.; Ribó, S.; Martín-Neira, M. First spaceborne phase altimetry over sea ice using TechDemoSat-1 GNSS-R signals. *Geophys. Res. Lett.* **2017**, *44*, 8369–8376. [CrossRef]
24. Li, W.; Cardellach, E.; Fabra, F.; Ribó, S.; Rius, A. Lake Level and Surface Topography Measured With Spaceborne GNSS-Reflectometry From CYGNSS Mission: Example for the Lake Qinghai. *Geophys. Res. Lett.* **2018**, *45*, 13,332–13,341. [CrossRef]
25. Mayers, D.; Ruf, C. Measuring Ice Thickness with Cygnss Altimetry. In Proceedings of the IGARSS 2018—2018 IEEE International Geoscience and Remote Sensing Symposium, Valencia, Spain, 22–27 July 2018; pp. 8535–8538.
26. Song, M.; He, X.; Wang, X.; Jia, D.; Xiao, R.; Shi, H.; Wu, Y. Study on the Exploration of Spaceborne GNSS-R Raw Data Focusing on Altimetry. *IEEE J. Sel. Top. Appl. Earth Observ. Remote Sens.* **2020**, *13*, 6142–6154. [CrossRef]
27. Morton, Y.J.; Wang, Y.; Yang, R. Coherent GNSS Reflection Signal Processing for Precision Altimetry Applications. In Proceedings of the IGARSS 2020—2020 IEEE International Geoscience and Remote Sensing Symposium, Waikoloa, HI, USA, 26 September–2 October 2020; pp. 3365–3368.
28. Wang, Y.; Breitsch, B.; Morton, Y.T.J. A State-Based Method to Simultaneously Reduce Cycle Slips and Noise in Coherent GNSS-R Phase Measurements From Open-Loop Tracking. *IEEE Trans. Geosci. Remote Sens.* **2021**, *59*, 8873–8884. [CrossRef]
29. Peng, J.; Li, W.; Cardellach, E.; Marigold, G.; Clarizia, M.P. Signal Coherence and Water Detection Algorithms for the ESA HydroGNSS Mission. *IEEE Trans. Geosci. Remote Sens.* **2024**, *62*, 5801218. [CrossRef]
30. Xie, J.; Bu, J.; Li, H.; Wang, Q. Spaceborne GNSS Reflectometry for Vegetation and Inland Water Monitoring: Progress, Challenges, Opportunities, and Potential. *Remote Sens.* **2025**, *17*, 1199. [CrossRef]
31. Unwin, M.; Jales, P.; Tye, J.; Gommenginger, C.; Foti, G.; Rosello, J. Spaceborne GNSS-reflectometry on TechDemoSat-1: Early mission operations and exploitation. *IEEE J. Sel. Top. Appl. Earth Observ. Remote Sens.* **2016**, *9*, 4525–4539. [CrossRef]
32. Ruf, C.; Chang, P.; Clarizia, M.; Gleason, S.; Jelenak, Z.; Murray, J.; Morris, M.; Musko, S.; Posselt, D.; Provost, D. *CYGNSS Handbook Cyclone Global Navigation Satellite System: Deriving Surface Wind Speeds in Tropical Cyclones*; National Aeronautics and Space Administration: Ann Arbor, MI, USA, 2016; Volume 154.
33. Sun, Y.; Wang, X.; Du, Q.; Bai, W.; Xia, J.; Cai, Y.; Wang, D.; Wu, C.; Meng, X.; Tian, Y. The status and progress of Fengyun-3E GNOS II mission for GNSS remote sensing. In Proceedings of the IGARSS 2019—2019 IEEE International Geoscience and Remote Sensing Symposium, Yokohama, Japan, 28 July–2 August 2019; pp. 5181–5184.
34. Sun, Y.; Huang, F.; Xia, J.; Yin, C.; Bai, W.; Du, Q.; Wang, X.; Cai, Y.; Li, W.; Yang, G.; et al. GNOS-II on Fengyun-3 Satellite Series: Exploration of Multi-GNSS Reflection Signals for Operational Applications. *Remote Sens.* **2023**, *15*, 5756. [CrossRef]
35. Jales, P. *Spaceborne Receiver Design for Scatterometric GNSS Reflectometry*; University of Surrey (UK): Guildford, UK, 2012.
36. King, L.S.; Unwin, M.; Rawlinson, J.; Guida, R.; Underwood, C. Processing of raw GNSS reflectometry data from TDS-1 in a backscattering configuration. *IEEE J. Sel. Top. Appl. Earth Obs. Remote Sens.* **2020**, *13*, 2916–2924. [CrossRef]
37. Mashburn, J.; Axelrad, P.; Lowe, S.T.; Larson, K.M. Global Ocean Altimetry With GNSS Reflections From TechDemoSat-1. *IEEE Trans. Geosci. Remote Sens.* **2018**, *56*, 4088–4097. [CrossRef]

38. Ren, X.; Liu, H.; Zhang, J.; Mei, D.; Zhang, X. An Improved Method for Ionospheric TEC Estimation Using the Spaceborne GNSS-R Observations. *IEEE Trans. Geosci. Remote Sens.* **2022**, *60*, 3192983. [CrossRef]
39. Ruf, C.S.; Atlas, R.; Chang, P.S.; Clarizia, M.P.; Garrison, J.L.; Gleason, S.; Katzberg, S.J.; Jelenak, Z.; Johnson, J.T.; Majumdar, S.J. New ocean winds satellite mission to probe hurricanes and tropical convection. *Bull. Am. Meteorol. Soc.* **2016**, *97*, 385–395. [CrossRef]
40. Carreno-Luengo, H.; Ruf, C.S.; Gleason, S.; Russel, A. A New Multiresolution CYGNSS Data Product for Fully and Partially Coherent Scattering. *IEEE Trans. Geosci. Remote Sens.* **2023**, *61*, 3318639. [CrossRef]
41. Carreno-Luengo, H.; Ruf, C.; Gleason, S.; Russel, A.; Butler, T. Generation of A New High Resolution Ddm Data Product from Cygnss Raw If Measurements. In Proceedings of the 2021 IEEE International Geoscience and Remote Sensing Symposium IGARSS, Brussels, Belgium, 11–16 July 2021; pp. 7815–7818.
42. Zhang, Y.; Yan, Z.; Yang, S.; Meng, W.; Han, Y.; Hong, Z. Feasibility study on Qinghai Lake Boundary detection using CYGNSS raw IF Data. *IEEE J. Sel. Top. Appl. Earth Obs. Remote Sens.* **2024**, *17*, 3290680. [CrossRef]
43. Cardellach, E.; Li, W.; Rius, A.; Semmling, M.; Wickert, J.; Zus, F.; Ruf, C.S.; Buontempo, C. First Precise Spaceborne Sea Surface Altimetry With GNSS Reflected Signals. *IEEE J. Sel. Top. Appl. Earth Obs. Remote Sens.* **2020**, *13*, 102–112. [CrossRef]
44. Molina, C.; Boudriki Semlali, B.-E.; Park, H.; Camps, A. A preliminary study on ionospheric scintillation anomalies detected using GNSS-R data from NASA CYGNSS mission as possible earthquake precursors. *Remote Sens.* **2022**, *14*, 2555. [CrossRef]
45. Al-Khaldi, M.M.; Johnson, J.T.; Chan, S.K.; Hajj, G. Near-Specular Interferometry With Signals of Opportunity Systems: Potential and Limitations. *IEEE Trans. Geosci. Remote Sens.* **2025**, *63*, 3550285. [CrossRef]
46. Jing, C.; Li, W.; Wan, W.; Lu, F.; Niu, X.; Chen, X.; Rius, A.; Cardellach, E.; Ribó, S.; Liu, B.; et al. A review of the BuFeng-1 GNSS-R mission: Calibration and validation results of sea surface and land surface. *Geo-Spat. Inf. Sci.* **2024**, *27*, 638–652. [CrossRef]
47. Nguyen, V.A.; Nogués-Correig, O.; Yuasa, T.; Masters, D.; Irisov, V. Initial GNSS Phase Altimetry Measurements From the Spire Satellite Constellation. *Geophys. Res. Lett.* **2020**, *47*, e2020GL088308. [CrossRef]
48. Wang, Y.; Morton, Y.J. Evaluation of GNSS-R Retrieved Sea Ice Surface Height Using ICESat-2 Ice Freeboard Measurements. In Proceedings of the 2021 IEEE International Geoscience and Remote Sensing Symposium IGARSS, Brussels, Belgium, 11–16 July 2021; pp. 7803–7806.
49. Wang, Y.; Morton, Y.J. Ionospheric total electron content and disturbance observations from space-borne coherent GNSS-R measurements. *IEEE Trans. Geosci. Remote Sens.* **2021**, *60*, 3093328. [CrossRef]
50. Wang, C.; Camps, A.; Hu, X.; Park, H.; Yu, K.; Zhai, X.; Lu, W.; Huang, F.; Liao, M.; Zhang, P.; et al. A Novel Geometry Agnostic Delay and Doppler Tracking Technique for GNSS-Reflectometry: Application to the GNOS-II Payload Onboard the FY-3E. *IEEE J. Sel. Top. Appl. Earth Obs. Remote Sens.* **2025**, *18*, 8040–8056. [CrossRef]
51. Wang, Y.; Morton, Y.J. Spaceborne GNSS-R for High Latitude Ionospheric TEC Disturbance Observations. In Proceedings of the 2021 IEEE Specialist Meeting on Reflectometry using GNSS and other Signals of Opportunity (GNSS+R), Beijing, China, 14–17 September 2021; pp. 21–24.
52. Roesler, C.J.; Morton, Y.J.; Wang, Y.; Nerem, R.S. Coherent GNSS-Reflections Characterization Over Ocean and Sea Ice Based on Spire Global CubeSat Data. *IEEE Trans. Geosci. Remote Sens.* **2022**, *60*, 3129999. [CrossRef]
53. Zhang, J.; Morton, Y.J.; Wang, Y.; Roesler, C.J. Mapping Surface Water Extents Using High-Rate Coherent Spaceborne GNSS-R Measurements. *IEEE Trans. Geosci. Remote Sens.* **2022**, *60*, 3218254. [CrossRef]
54. Buendía, R.N.; Tabibi, S.; Talpe, M.; Otosaka, I. Ice sheet height retrievals from Spire grazing angle GNSS-R. *Remote Sens. Environ.* **2023**, *297*, 113757. [CrossRef]
55. Carreno-Luengo, H.; Camps, A.; Via, P.; Munoz, J.F.; Cortiella, A.; Vidal, D.; Jané, J.; Catarino, N.; Hagenfeldt, M.; Palomo, P. 3Cat-2—An experimental nanosatellite for GNSS-R earth observation: Mission concept and analysis. *IEEE J. Sel. Top. Appl. Earth Observ. Remote Sens.* **2016**, *9*, 4540–4551. [CrossRef]
56. Carreno-Luengo, H.; Lowe, S.; Zuffada, C.; Esterhuizen, S.; Oveisgharan, S. Spaceborne GNSS-R from the SMAP mission: First assessment of polarimetric scatterometry over land and cryosphere. *Remote Sens.* **2017**, *9*, 362. [CrossRef]
57. Masters, D. Design and planning for the first spire GNSS-R missions of 2019. In Proceedings of the IEEE GRSS, Spec. Meeting Reflectometry Using GNSS Other Signals Opportunity, Benevento, Italy, 20–22 May 2019.
58. Masters, D.; Irisov, V.; Nguyen, V.; Duly, T.; Nogués-Correig, O.; Tan, L.; Yuasa, T.; Ringer, J.; Sikarin, R.; Gorbunov, M. Status and plans for Spire's growing commercial constellation of GNSS science cubeSats. In Proceedings of the Joint 6th ROM SAF User Workshop and 7th IROWG Workshop, Helsingør, Denmark, 19–25 September 2019; pp. 19–25.
59. Freeman, V.; Masters, D.; Jales, P.; Esterhuizen, S.; Ebrahimi, E.; Irisov, V.; Ben Khadhra, K. Earth Surface Monitoring with Spire's New GNSS Reflectometry (GNSS-R) CubeSats. In Proceedings of the EGU General Assembly Conference Abstracts, In Virtual, 4–8 May 2020; p. 13766.

60. Munoz-Martin, J.F.; Miguelez, N.; Castella, R.; Fernandez, L.; Solanellas, A.; Via, P.; Camps, A. 3Cat-4: Combined GNSS-R, L-Band radiometer with RFI mitigation, and AIS receiver for a I-Unit Cubesat based on software defined radio. In Proceedings of the IGARSS 2018-2018 IEEE International Geoscience and Remote Sensing Symposium, Valencia, Spain, 22–27 July 2018; pp. 1063–1066.
61. Dielacher, A.; Fragner, H.; Moritsch, M.; Høeg, P.; Wickert, J.; Cardellach, E.; Koudelka, O.; Beck, P.; Walker, R.; Martin-Neira, M. The passive reflectometer on board of PRETTY. In Proceedings of the ESA ARSIKEO Conference, Noordwijk, The Netherlands, 11–13 November 2019.
62. Juang, J.-C.; Ma, S.-H.; Lin, C.-T. Study of GNSS-R techniques for FORMOSAT mission. *IEEE J. Sel. Top. Appl. Earth Observ. Remote Sens.* **2016**, *9*, 4582–4592. [CrossRef]
63. Wang, H.Y.; Juang, J.C. Retrieval of Ocean Surface Wind Speed Using Reflected BPSK/BOC Signals. *Remote Sens.* **2020**, *12*, 2698. [CrossRef]
64. Peng, J.; Cardellach, E.; Li, W.; Ribó, S.; Rius, A. Toward the Exploitation of HydroGNSS Coherent Channel: High Sampling Rate Products. *IEEE Trans. Geosci. Remote Sens.* **2025**, *63*, 3554191. [CrossRef]
65. Liu, X.; Bu, J.; Zuo, X.; Wang, Z.; Wang, Q.; Wang, Q.; Ji, C.; Zhao, Y.; Yang, H.; He, X. Performance Validation of Sea Surface Wind Speed Retrieval Algorithms and Products From the Chinese Tianmu-1 Constellation GNSS-R: First Results on Comparison With Other Wind Speed Products. *IEEE J. Sel. Top. Appl. Earth Obs. Remote Sens.* **2025**, *18*, 5189–5203. [CrossRef]
66. Wang, Y.; Morton, Y.J. Coherent GNSS Reflection Signal Processing for High-Precision and High-Resolution Spaceborne Applications. *IEEE Trans. Geosci. Remote Sens.* **2021**, *59*, 831–842. [CrossRef]
67. Beckmann, P.; Spizzichino, A. *The Scattering of Electromagnetic Waves from Rough Surfaces*; Artech House, Inc.: Norwood, MA, USA, 1963.
68. Chen, W.-K. *The Electrical Engineering Handbook*; Elsevier: Amsterdam, The Netherlands, 2004.
69. Wang, Y.; Morton, Y.J. Coherent Reflections Using Closed-Loop PLL Processing of CYGNSS IF Data. In Proceedings of the IGARSS 2019—2019 IEEE International Geoscience and Remote Sensing Symposium, Yokohama, Japan, 28 July–2 August 2019; pp. 8737–8740.
70. Wang, Y.; Morton, Y. Coherent components of GNSS-R signal observed from CYGNSS raw IF data. In Proceedings of the 32nd International Technical Meeting of the Satellite Division of The Institute of Navigation (ION GNSS+ 2019), Miami, FL, USA, 16–20 September 2019; pp. 3319–3326.
71. Fisher, N.I. *Statistical Analysis of Circular Data*; Cambridge University Press: Cambridge, UK, 1993.
72. Roesler, C.; Wang, Y.; Morton, Y.J.; Nerem, R.S. Coherent GPS Reflections Over Ocean Surface. In Proceedings of the IGARSS 2020—2020 IEEE International Geoscience and Remote Sensing Symposium, Waikoloa, HI, USA, 26 September–2 October 2020; pp. 6218–6221.
73. Wang, Y.; Liu, Y.; Roesler, C.; Morton, Y.J. Detection of Coherent GNSS-R Measurements Using a Support Vector Machine. In Proceedings of the IGARSS 2020—2020 IEEE International Geoscience and Remote Sensing Symposium, Waikoloa, HI, USA, 26 September–2 October 2020; pp. 6210–6213.
74. Loria, E.; Russo, I.M.; Wang, Y.; Giangregorio, G.; Galdi, C.; Bisceglie, M.d.; Wilson-Downs, B.; Lavalle, M.; O'Brien, A.J.; Morton, Y.J.; et al. Comparison of GNSS-R Coherent Reflection Detection Algorithms Using Simulated and Measured CYGNSS Data. *IEEE Trans. Geosci. Remote Sens.* **2023**, *61*, 3277411. [CrossRef]
75. Chew, C.; Shah, R.; Zuffada, C.; Hajj, G.; Masters, D.; Mannucci, A.J. Demonstrating soil moisture remote sensing with observations from the UK TechDemoSat-1 satellite mission. *Geophys. Res. Lett.* **2016**, *43*, 3317–3324. [CrossRef]
76. Chew, C.C.; Zuffada, C.; Shah, R.; Mannucci, A.J. Mapping sea ice using reflected GNSS signals in a bistatic radar system. In Proceedings of the EGU General Assembly 2016, Vienna, Austria, 17–22 April 2016.
77. Nghiem, S.V.; Zuffada, C.; Shah, R.; Chew, C.; Lowe, S.T.; Mannucci, A.J.; Cardellach, E.; Brakenridge, G.R.; Geller, G.; Rosenqvist, A. Wetland monitoring with Global Navigation Satellite System reflectometry. *Earth Space Sci.* **2017**, *4*, 16–39. [CrossRef] [PubMed]
78. Yan, Q.; Huang, W. Spaceborne GNSS-R Sea Ice Detection Using Delay-Doppler Maps: First Results From the U.K. TechDemoSat-1 Mission. *IEEE J. Sel. Top. Appl. Earth Obs. Remote Sens.* **2016**, *9*, 4795–4801. [CrossRef]
79. Al-Khaldi, M.M.; Johnson, J.T.; Gleason, S.; Chew, C.C.; Gerlein-Safdi, C.; Shah, R.; Zuffada, C. Inland Water Body Mapping Using CYGNSS Coherence Detection. *IEEE Trans. Geosci. Remote Sens.* **2021**, *59*, 7385–7394. [CrossRef]
80. Russo, I.M.; Bisceglie, M.d.; Galdi, C.; Lavalle, M.; Zuffada, C. Entropy-Based Coherence Metric for Land Applications of GNSS-R. *IEEE Trans. Geosci. Remote Sens.* **2022**, *60*, 3125858. [CrossRef]
81. Collett, I.; Wang, Y.; Shah, R.; Roesler, C.; Morton, Y.J. GPS Signal Land Reflection Coherence Dependence on Water Extent and Surface Topography using Cygnss Measurements. In Proceedings of the IGARSS 2020—2020 IEEE International Geoscience and Remote Sensing Symposium, Waikoloa, HI, USA, 26 September–2 October 2020; pp. 6206–6209.
82. Collett, I.; Wang, Y.; Shah, R.; Morton, Y.J. Phase Coherence of GPS Signal Land Reflections and its Dependence on Surface Characteristics. *IEEE Geosci. Remote Sens. Lett.* **2022**, *19*, 3094407. [CrossRef]

83. Liu, Q.; Li, W.; Zhang, S.; Nan, Y.; Peng, J.; Ma, Z. Analysis of signal-to-noise ratio retrieved from multi-GNSS satellite data of land surface reflections. *GPS Solut.* **2023**, *27*, 151. [CrossRef]
84. Nan, Y.; Ye, S.; Liu, J.; Guo, B.; Zhang, S.; Li, W. Signal-to-Noise Ratio Analyses of Spaceborne GNSS-Reflectometry from Galileo and BeiDou Satellites. *Remote Sens.* **2022**, *14*, 35. [CrossRef]
85. Zhu, Y.; Guo, F.; Zhang, X. Spaceborne GNSS-R soil moisture retrieval from GPS/BDS-3/Galileo satellites. *GPS Solut.* **2024**, *29*, 10. [CrossRef]
86. Du, H.; Nan, Y.; Li, W.; Cardellach, E.; Ribó, S.; Rius, A. Coherent Combination of GPS III L1 C/A and L1C Signals for GNSS Reflectometry. *IEEE Trans. Geosci. Remote Sens.* **2024**, *62*, 3398435. [CrossRef]
87. Tranvik, L.J.; Downing, J.A.; Cotner, J.B.; Loiselle, S.A.; Striegl, R.G.; Ballatore, T.J.; Dillon, P.; Finlay, K.; Fortino, K.; Knoll, L.B.; et al. Lakes and reservoirs as regulators of carbon cycling and climate. *Limnol. Oceanogr.* **2009**, *54*, 2298–2314. [CrossRef]
88. Pickens, A.H.; Hansen, M.C.; Hancher, M.; Stehman, S.V.; Tyukavina, A.; Potapov, P.; Marroquin, B.; Sherani, Z. Mapping and sampling to characterize global inland water dynamics from 1999 to 2018 with full Landsat time-series. *Remote Sens. Environ.* **2020**, *243*, 111792. [CrossRef]
89. Vanderhoof, M.K.; Alexander, L.; Christensen, J.; Solvik, K.; Nieuwlandt, P.; Sagehorn, M. High-frequency time series comparison of Sentinel-1 and Sentinel-2 satellites for mapping open and vegetated water across the United States (2017–2021). *Remote Sens. Environ.* **2023**, *288*, 113498. [CrossRef] [PubMed]
90. Scott, M.; Chew, C.; Wang, Y.; Roesler, C.; Morton, Y.J. On The Relationship Between The GNSS-R Signal SNR and Coherency With Surface Water: A Case Study Over Lake Okeechobee. In Proceedings of the IGARSS 2023—2023 IEEE International Geoscience and Remote Sensing Symposium, Pasadena, CA, USA, 16–21 July 2023; pp. 3345–3348.
91. Carreno-Luengo, H.; Ruf, C.S.; Gleason, S.; Russel, A. Detection of inland water bodies under dense biomass by CYGNSS. *Remote Sens. Environ.* **2024**, *301*, 113896. [CrossRef]
92. Li, W.; Cardellach, E.; RibÓ, S.; Rius, A.; Zhou, B. First spaceborne demonstration of BeiDou-3 signals for GNSS reflectometry from CYGNSS constellation. *Chin. J. Aeronaut.* **2021**, *34*, 1–10. [CrossRef]
93. Mei, J.; Yan, S.; Chen, C. Multifeature Water Discrimination Method Based on CYGNSS Intermediate Frequency Data. *IEEE Trans. Geosci. Remote Sens.* **2025**, *63*, 3531636. [CrossRef]
94. Wang, Y.; Morton, Y.J. River Slope Observation From Spaceborne GNSS-R Carrier Phase Measurements: A Case Study. *IEEE Geosci. Remote Sens. Lett.* **2022**, *19*, 3127750. [CrossRef]
95. Wang, Y.; Morton, Y.J. Observation of the Mississippi River Surface Gradients from Spire's GNSS-R CubeSats. In Proceedings of the IGARSS 2022—2022 IEEE International Geoscience and Remote Sensing Symposium, Kuala Lumpur, Malaysia, 17–22 July 2022; pp. 4403–4406.
96. Nielsen, K.; Stenseng, L.; Andersen, O.B.; Villadsen, H.; Knudsen, P. Validation of CryoSat-2 SAR mode based lake levels. *Remote Sens. Environ.* **2015**, *171*, 162–170. [CrossRef]
97. Yanez, C.; Li, W.; Cardellach, E.; Raynal, M.; Picot, N.; Martin-Neira, M.; Borde, F. Lake Water Level Estimation from Grazing GNSS-Reflectometry and Satellite Radar Altimetry over the Great Lakes. *IEEE Geosci. Remote Sens. Lett.* **2024**, *21*, 1–5. [CrossRef]
98. Zhang, J.; Morton, Y.J. Inland Water Body Surface Height Retrievals Using CYGNSS Delay Doppler Maps. *IEEE Trans. Geosci. Remote Sens.* **2023**, *61*, 3330410. [CrossRef]
99. Pavlis, N.K.; Holmes, S.A.; Kenyon, S.C.; Factor, J.K. The development and evaluation of the Earth Gravitational Model 2008 (EGM2008). *J. Geophys. Res. Solid Earth* **2012**, *117*. [CrossRef]
100. Semmling, A.M.; Beckheinrich, J.; Wickert, J.; Beyerle, G.; Schön, S.; Fabra, F.; Pflug, H.; He, K.; Schwabe, J.; Scheinert, M. Sea surface topography retrieved from GNSS reflectometry phase data of the GEOHALO flight mission. *Geophys. Res. Lett.* **2014**, *41*, 954–960. [CrossRef]
101. Clarizia, M.P.; Ruf, C.; Cipollini, P.; Zuffada, C. First spaceborne observation of sea surface height using GPS-Reflectometry. *Geophys. Res. Lett.* **2016**, *43*, 767–774. [CrossRef]
102. Hu, C.; Benson, C.; Rizos, C.; Qiao, L. Single-Pass Sub-Meter Space-Based GNSS-R Ice Altimetry: Results From TDS-1. *IEEE J. Sel. Top. Appl. Earth Obs. Remote Sens.* **2017**, *10*, 3782–3788. [CrossRef]
103. Li, W.; Rius, A.; Fabra, F.; Cardellach, E.; Ribo, S.; Martin-Neira, M. Revisiting the GNSS-R Waveform Statistics and Its Impact on Altimetric Retrievals. *IEEE Trans. Geosci. Remote. Sens.* **2018**, *56*, 2854–2871. [CrossRef]
104. Mashburn, J.; Axelrad, P.; Zuffada, C.; Loria, E.; O'Brien, A.; Haines, B. Improved GNSS-R Ocean Surface Altimetry With CYGNSS in the Seas of Indonesia. *IEEE Trans. Geosci. Remote Sens.* **2020**, *58*, 6071–6087. [CrossRef]
105. Cardellach, E.; Ao, C.O.; de la Torre Juárez, M.; Hajj, G.A. Carrier phase delay altimetry with GPS-reflection/occultation interferometry from low Earth orbiters. *Geophys. Res. Lett.* **2004**, *31*. [CrossRef]
106. Semmling, A.M.; Schmidt, T.; Wickert, J.; Schön, S.; Fabra, F.; Cardellach, E.; Rius, A. On the retrieval of the specular reflection in GNSS carrier observations for ocean altimetry. *Radio Sci.* **2012**, *47*, 1–13. [CrossRef]
107. Parrinello, T.; Shepherd, A.; Bouffard, J.; Badessi, S.; Casal, T.; Davidson, M.; Fornari, M.; Maestroni, E.; Scagliola, M. CryoSat: ESA's ice mission—Eight years in space. *Adv. Space Res.* **2018**, *62*, 1178–1190. [CrossRef]

108. Wang, Y.; Morton, Y.J.; Minear, J.T.; Putnam, A.; Conrad, A.; Axelrad, P.; Nerem, R.S.; Warnock, A.; Ruf, C.; Moreira, D.M.; et al. Measuring river slope using spaceborne GNSS reflectometry: Methodology and first performance assessment. *Remote Sens. Environ.* **2025**, *318*, 114597.
109. Ren, X.; Liu, H.; Mei, D.; Yang, P.; Zhang, Z.; Freeshah, M.; Zhang, X. Leveraging the CYGNSS Spaceborne GNSS-R Observations to Detect Ionospheric Irregularities Over the Oceans: Method and Verification. *Space Weather* **2022**, *20*, e2022SW003141. [CrossRef]
110. Ren, X.; Zhang, J.; Chen, J.; Zhang, X. Global Ionospheric Modeling Using Multi-GNSS and Upcoming LEO Constellations: Two Methods and Comparison. *IEEE Trans. Geosci. Remote Sens.* **2022**, *60*, 1–15. [CrossRef]
111. Molina, C.; Camps, A. First Evidences of Ionospheric Plasma Depletions Observations Using GNSS-R Data from CYGNSS. *Remote Sens.* **2020**, *12*, 3782. [CrossRef]
112. Camps, A.; Park, H.; Foti, G.; Gommenginger, C. Ionospheric Effects in GNSS-Reflectometry From Space. *IEEE J. Sel. Top. Appl. Earth Obs. Remote Sens.* **2016**, *9*, 5851–5861. [CrossRef]
113. Camps, A.; Park, H.; Juan, J.M.; Sanz, J.; Gonzalez-Casado, G.; Barbosa, J.; Fabbro, V.; Lemorton, J.; Orus, R. *Ionospheric scintillation monitoring using GNSS-R?, Proceedings of the 38th Annual IEEE International Geoscience and Remote Sensing Symposium, IGARSS 2018, Valencia, Spain, 22–27 July 2018*; Institute of Electrical and Electronics Engineers Inc.: Valencia, Spain, 2018; pp. 3339–3342.
114. Moreno, M.; Semmling, M.; Stienne, G.; Hoque, M.; Wickert, J. Characterizing Ionospheric Effects on GNSS Reflectometry at Grazing Angles from Space. *Remote Sens.* **2023**, *15*, 5049. [CrossRef]
115. Wang, Y.; Morton, Y.J. Polar Ionospheric TEC Enhancement Observation Using GNSS-R. In Proceedings of the 2023 XXXVth General Assembly and Scientific Symposium of the International Union of Radio Science (URSI GASS), Sapporo, Japan, 19–26 August 2023; pp. 1–4.
116. Priyadarshi, S. A review of ionospheric scintillation models. *Surv. Geophys.* **2015**, *36*, 295–324. [CrossRef]
117. Wu, Y.; Jiang, N.; Xu, Y.; Yeh, T.-K.; Xu, T.; Wang, Y.; Su, W. Improving the capability of water vapor retrieval from Landsat 8 using ensemble machine learning. *Int. J. Appl. Earth Obs. Geoinf.* **2023**, *122*, 103407. [CrossRef]
118. Li, Q.; Böhm, J.; Yuan, L.; Weber, R. Global zenith wet delay modeling with surface meteorological data and machine learning. *GPS Solut.* **2024**, *28*, 57. [CrossRef]
119. Landskron, D.; Böhm, J. VMF3/GPT3: Refined discrete and empirical troposphere mapping functions. *J. Geod.* **2018**, *92*, 349–360. [CrossRef]
120. Li, Q.; Yuan, L.; Jiang, Z. Modeling tropospheric zenith wet delays in the Chinese mainland based on machine learning. *GPS Solut.* **2023**, *27*, 171. [CrossRef]
121. Wang, Y. Troposphere Sensing Using Grazing-Angle GNSS-R Measurement From LEO Satellites. *Geophys. Res. Lett.* **2023**, *50*, e2023GL106249. [CrossRef]
122. Jaberi Shafei, M.; Mashhadi-Hossainali, M. Application of the GNSS-R in tomographic sounding of the Earth atmosphere. *Adv. Space Res.* **2018**, *62*, 71–83. [CrossRef]
123. Scott, M.; Roesler, C.; Wang, Y.; Morton, Y.; Nerem, S. Tropospheric error budget for GNSS-R altimetry at low grazing angles. In Proceedings of the Proceedings of the 34th International Technical Meeting of the Satellite Division of The Institute of Navigation (ION GNSS+ 2021), St. Louis, MO, USA, 20–24 September 2021; pp. 4021–4029.
124. Moreno, M.; Semmling, M.; Stienne, G.; Dalil, W.; Hoque, M.; Wickert, J.; Reboul, S. Airborne Coherent GNSS Reflectometry and Zenith Total Delay Estimation over Coastal Waters. *Remote Sens.* **2022**, *14*, 4628. [CrossRef]
125. Wang, Y. Grazing-angle GNSS-R for the determination of tropospheric delay and water vapor content. In *Proceedings of the Proceedings of the 36th International Technical Meeting of the Satellite Division of The Institute of Navigation (ION GNSS+ 2023)*; Denver, CO, USA, 11–15 September 2023, pp. 3227–3232.
126. Roesler, C.; Morton, Y.J. Retrieving Atmospheric Water Vapor Content from Grazing Angle GNSS Reflectometry Measurements: Methodology and Performance Assessment. *TechRxiv* **2025**. [CrossRef]
127. Anderson, S.G.; Wang, Y.; Morton, Y.J. Relating GNSS Reflected Signal Coherence to Ice Shelf Surface Deformation and Roughness. *IEEE Trans. Geosci. Remote Sens.* **2025**, *63*, 3538558. [CrossRef]

Disclaimer/Publisher's Note: The statements, opinions and data contained in all publications are solely those of the individual author(s) and contributor(s) and not of MDPI and/or the editor(s). MDPI and/or the editor(s) disclaim responsibility for any injury to people or property resulting from any ideas, methods, instructions or products referred to in the content.